



1 **Integrating field, textural and geochemical monitoring to track eruption triggers and**  
2 **dynamics: a case-study from Piton de la Fournaise**

3

4 Lucia Gurioli<sup>(1)</sup>, Andrea Di Muro<sup>(2)</sup>, Ivan Vlastélic<sup>(1)</sup>, Séverine Moune<sup>(1)</sup>, Nicolas  
5 Villeneuve<sup>(2)</sup>, Patrick Bachèlery<sup>(1)</sup>, Marina Valer<sup>(1)</sup>, Simon Thivet<sup>(1)</sup>, Guillaume Boudoire<sup>(2,3)</sup>,  
6 Aline Peltier<sup>(2)</sup>, Valerie Ferrazzini<sup>(2)</sup>, Nicole Métrich<sup>(2)</sup>, Mhammed Benbakkar<sup>(1)</sup>, Nicolas  
7 Cluzel<sup>(1)</sup>, Christophe Constantin<sup>(1)</sup>, Jean-Luc Devidal<sup>(1)</sup>, Claire Fonquernie<sup>(1)</sup>, Jean-Marc  
8 Hénot<sup>(1)</sup>

9 (1) Université Clermont Auvergne, CNRS, IRD, OPGC, Laboratoire Magmas et Volcans, F-63000  
10 Clermont-Ferrand, France

11 (2) Institut de Physique du Globe (IPGP), Sorbonne Paris-Cite, CNRS UMR-7154, Université Paris  
12 Diderot, Observatoire Volcanologique du Piton de la Fournaise (OVPF), Bourg Murat, France,

13 (3) Laboratoire Géosciences Réunion, Université de La Réunion, Institut de Physique du Globe de  
14 Paris, Sorbonne Paris-Cité, UMR 7154 CNRS, F-97715 Saint-Denis, France

15 Corresponding author: L Gurioli, Université Clermont Auvergne, CNRS, IRD, OPGC, LMV  
16 Campus Universitaire des Cézeaux 6 Avenue Blaise Pascal 63178 Aubière Cedex  
17 ([lucia.guriolica.fr](mailto:lucia.guriolica.fr))

18

19 **Abstract**

20 The 2014 eruption at Piton de La Fournaise (PdF), la Reunion, which occurred after 41  
21 months of quiescence, began with surprisingly little precursory activity, and was one of the  
22 smallest so far observed at PdF in terms of duration (less than 2 days) and volume (less than  
23 0.4 Mm<sup>3</sup>). The pyroclastic material was composed of spiny-opaque, spiny-iridescent, and  
24 fluidal scoria along with golden pumice. Density analyses performed on 200 lapilli reveal that  
25 the spiny-opaque clasts are the densest (1600 kg/m<sup>3</sup>) and richest in crystals (54 vol%), and the  
26 golden pumices are the lightest (400 kg/m<sup>3</sup>) and poorest in crystals (14 vol%). The  
27 connectivity data indicate that the fluidal and golden (Hawaiian-like) clasts have more  
28 isolated vesicles (up to 40%) than the spiny (Strombolian-like) clasts (0-5%). These textural  
29 variations are linked to primary pre-eruptive magma storage conditions. The golden and  
30 fluidal fragments track the hotter portion of the melt, in contrast to the spiny fragments which  
31 mirror the cooler portion of the shallow reservoir. Progressive tapping of these distinct



32 portions leads to a decrease in the explosive intensity from early fountaining to Strombolian  
33 activity. The geochemical results confirm the absence of new hot input of magma and confirm  
34 the involvement of a single, shallow, differentiated magma source, possibly related to residual  
35 magma from the November 2009 eruption. We found that the eruption was triggered by water  
36 exsolution, favoured by the shallow depth of the reservoir, rather than cooling and chemical  
37 evolution of the stored magma.

38

39 **Key words** : Piton de La Fournaise, Hawaiian activity, Strombolian activity, shallow reservoir,  
40 texture, petrology, geochemistry

41

## 42 **1. Introduction**

43

44 A detailed characterization and understanding of eruptive dynamics and of processes driving  
45 and modulating volcano unrest is crucial in monitoring active volcanoes and fundamental for  
46 forecasting volcanic eruptions (Sparks, 2003). Many studies suggest that eruptive phenomena  
47 are strongly dependent on the physico-chemical properties of ascending magma in the conduit  
48 (e.g., temperature, viscosity, porosity, and permeability) (e.g. Sparks, 1978; Rust and  
49 Cashman, 2011; Gonnermann and Manga, 2013; Polacci et al., 2014). Integrating  
50 petrographic, chemical and textural data can thus provide critical information to constrain  
51 both the pre-eruptive storage conditions, and the processes related to magma ascent, degassing  
52 and cooling (e.g., reference in Table 1 in Gurioli et al., 2015). This multidisciplinary approach  
53 is of even greater importance in the monitoring of volcanoes which emit relatively  
54 unchanging magma compositions over time, like basaltic volcanoes (e.g. Di Muro et al., 2014;  
55 Gurioli et al., 2015; Coppola et al., 2017). As a result, monitoring of textures, and  
56 petrochemical properties of lava fragments and pyroclasts is now routinely carried out on a  
57 daily basis at active volcanoes such as Kilauea, Etna, and Stromboli (e.g., Thornber et al.,  
58 2003; Polacci et al., 2006; Swanson et al., 2009; Tadeucci et al., 2002; Colo' et al., 2010;  
59 Houghton et al., 2011; 2013; 2016; Carey et al., 2012; 2013; Lautze et al., 2012; Andronico et  
60 al., 2013a; b; 2014; Corsaro and Miraglia, 2014; Di Muro et al., 2014; Eychienne et al.,  
61 2015; Gurioli et al.; 2014; Leduc et al., 2015; Le Pennec and Leibrandt, 2015; Kahl et al.,  
62 2015). In the past, time series of petrographic and geochemical data have been measured for  
63 Piton de la Fournaise (PdF) basalts and particularly for effusive products. The aim of these  
64 datasets was to constrain potential magma evolution for one of the most active basaltic  
65 volcanoes of the world (e.g. Albarède et al., 1997; Vlastélic et al., 2005; 2007, 2009; Vlastélic



66 and Pietruszka, 2016; Schiano et al., 2012; Boivin and Bachèlery, 2009; Peltier et al., 2009;  
67 Lénat et al., 2012; Di Muro et al., 2014; 2015). However, this type of approach has seldom  
68 been coupled with detailed textural studies at PdF and instead has mostly focused on crystal  
69 textures and crystal size distribution (Welsch et al., 2009; 2013; Di Muro et al., 2014; 2015).  
70 Moreover, only sporadic data exist on the textures of pyroclasts ejected by the PdF (Villemant  
71 et al., 2009; Famin et al., 2009; Michon et al., 2013; Vlastelic et al., 2013; Welsch et al., 2009;  
72 2013; Morandi et al., 2015; Di Muro et al., 2015; Ort et al., 2016).

73 Within this paper, we present a multidisciplinary textural, chemical and petrological  
74 approach to quantify and understand the short-lived 2014 PdF eruption. This approach  
75 combines detailed study of the pyroclastic deposit (grainsize and componentry) with bulk  
76 texture analysis (density, vesicularity, connectivity, morphology, vesicle distribution and  
77 crystal content) and a petro-chemical study (bulk rock, glass, minerals, melt inclusions) of the  
78 same clasts. This integrated approach has now been formalized within the National  
79 Observation Service for Volcanology (SNOV) as routine observational systems (DynVolc,  
80 Dynamics of Volcanoes, <http://wwwobs.univ-bpclermont.fr/SO/televolc/dynvolc/> and  
81 GazVolc, Observation des gaz volcaniques, <http://wwwobs.univ-bpclermont.fr/SO/televolc/gazvolc/>) to provide data for the on-going activity at PdF (Harris et  
82 al., 2017).  
83

84 In spite of being the first of a series of eruptions, the June 2014 event was preceded by  
85 only weak inflation and by a rapid increase in number of shallow (< 2 km below volcano  
86 summit) volcano tectonic earthquakes that happened only 11 days before the eruption (Peltier  
87 et al., 2016). The eruptive event was dominantly effusive, lasted only 20 hours and emitted a  
88 very small volume of magma (ca. 0.4 Mm<sup>3</sup>, Peltier et al., 2016), which makes this event one  
89 of the smallest, in terms of duration and volume, observed at PdF up to now. In addition, the  
90 eruption started during the night and very little direct observation exists for the first few hours  
91 of the activity, when the lava effusion was associated with very weak fountaining activity and  
92 Strombolian explosions.

93 This eruption occurred just outside the southern border of the summit Dolomieu  
94 caldera, at the top of the central cone of PdF (Fig. 1). This is a high risk sector because of the  
95 high number of tourists. Identification of precursors of this kind of activity represents an  
96 important challenge for monitoring systems (Bachèlery et al., 2016).

97 Therefore this eruption represents an ideal context to apply our multidisciplinary  
98 approach, with the aim of addressing the following key questions:

99 (i) why was such a small volume of magma erupted instead of forming an



- 100 intrusion?
- 101 (ii) what caused the rapid trigger and the sudden end to this small volume  
102 eruption?
- 103 (iii) which was the source of the eruption (shallow versus deep, single versus  
104 multiple small magma batches)? what was the ascent and degassing history of the  
105 magma? what was the time and space evolution of the eruptive event?

106 Furthermore, this eruption provides an exceptional opportunity to study processes  
107 leading to the transition from mild Hawaiian (<20 m high fountains, following the  
108 nomenclature proposed by Stovall et al., 2011) to Strombolian activity, whose products are  
109 little modified by post-fragmentation processes because of the very low intensity of the  
110 activity.

111 Finally, with these results we want to stress how combined textural and petro-chemical  
112 quantification of the eruptive products can be used to characterize on-going activity, and to  
113 provide valuable information to understand both the causes and the dynamics of potentially  
114 harmful eruptions.

115

## 116 **2 The 2014 activity**

### 117 **2.1 Precursory activity**

118 The 20 June 2014 summit eruption represents the first eruption at PdF after 41 months of  
119 quiescence. The last previous eruption had been on 9 December 2010, with a shallow (above  
120 sea level) intrusion on 2 February 2011 (Roult et al., 2012). From 2011, the deformation at  
121 PdF was constant with two distinct types of behaviour: (i) a summit contraction of a few  
122 centimetres every year; (ii) a preferential displacement of the east flank at a rate of 1-3  
123 centimetres per year (Brenquier et al., 2012; Staudacher and Peltier, 2015). The background  
124 microseismicity was very low (< 5 shallow events/day below volcano summit) and low-  
125 temperature summit intracaldera fumaroles emitted very little sulphur (H<sub>2</sub>S or SO<sub>2</sub>) and  
126 carbon (CO<sub>2</sub>) (Di Muro et al., 2012; 2016). After 41 months of rest, a new intense cycle of  
127 activity (June 2014, February 2015, May 2015, July 2015, August-October 2015; May 2016;  
128 September 2016; January 2017 and the on-going eruption that had started the 14 of July 2017)  
129 began with surprisingly little precursory activity.

130 The 2014 summit eruption started during the night of June 20/21, at 21h35 GMT (0h35 local  
131 time) and ended on June 21 at 17h09 GMT (21h09 local time), after less than 20 hours of  
132 dominantly effusive activity. The volcano reawakening was preceded, in March and April



133 2014, by deep (15-20 km below sea level) eccentric seismicity and increase in soil CO<sub>2</sub> flux  
134 below the western volcano flank, 15 km NW of the volcano summit (Liuzzo et al., 2015;  
135 Boudoire et al., 2017). Background microseismicity and inflation of the central cone increased  
136 progressively starting on 9 June 2014. On June 13, 17 and 20, three shallow (above sea level)  
137 intense seismic crises occurred below the summit Dolomieu caldera (Fig. 1), with hundreds of  
138 events located in a narrow depth range between 1100 and 2100 metres below the volcano  
139 summit. These seismic crises consisted of swarms of low magnitude ( $M$ : 1-2) volcano  
140 tectonic events which increased in number from the first to the third crisis. On June 20,  
141 seismicity increased progressively and a final seismic crisis started at 20h20 GMT, only 75  
142 minutes before the eruption. This seismic crisis was coupled with acceleration in the  
143 deformation of the summit area, which began only 60 minutes before the eruption.  
144 Interestingly, only slight inflation of the central cone ( $< 2$  cm of dilatation) was detected 11  
145 days before the 2014 eruption with a maximum of 1 cm and 1.6 cm enlargement at the  
146 summit and the base of the cone, respectively (Peltier et al., 2016). A moderate increase in  
147 CO<sub>2</sub> and H<sub>2</sub>S emissions from summit intracaldera fumaroles was detected starting on June 2,  
148 but only very minor SO<sub>2</sub> emissions occurred before the eruption (mostly on June 7 and 15,  
149 unpublished data). Therefore, the increase in both geophysical and geochemical parameters  
150 was mostly related to the late phase of injection of the dyke towards the surface. Following  
151 the end of the June 20-21 eruption, a long-term continuous inflation of the edifice began, at a  
152 moderate rate, and mostly at the base of the volcano. More than one year after this first  
153 eruption, the long-term deformation trends showed that the 2014 eruption marked a kink  
154 between the deflation trend which followed the caldera-forming 2007 eruption (Staudacher et  
155 al., 2009) and the currently ongoing continuous inflation trend (Peltier et al., 2016; Coppola et  
156 al., 2017).

157

## 158 **2.2 Chronology of the events and sampling strategies**

159 We reconstructed the chronology of events by combining a distribution map of the fissures,  
160 pyroclastic deposits and lava flows (Fig. 1) with a review of available images (visible and IR)  
161 and videos extracted from the observatory data base, the local newspapers, and web sites (Fig.  
162 2). The 2014 eruption occurred at the summit and on the SE slopes (Figs. 2a and 2b) of the  
163 central cone and evolved quickly and continuously over 20 hours. The full set of fractures  
164 opened during a short period of time (minutes) and emitted short ( $< 1.7$  km long) lava flows



165 (Fig. 1 and Figs. 2c and 2d). Feeding vents were scattered along a 0.6 km long fissure set (Fig.  
166 1) and produced very weak (low) Hawaiian to Strombolian activity (Fig. 2).

167 Fissures opened from west to east, initially sub-parallel to the southern border of  
168 Dolomieu caldera and then propagated at lower altitude (Fig. 1). The summit part of the  
169 fractures (ca. 2500 m asl, Western Fracture, Fig. 1) emitted only small volumes of lava and  
170 pyroclasts. This part of the fracture set was active only during the first few hours of the  
171 eruption, at night. The eastern part of the fractures (Upper Fracture, Fig. 1) descended to  
172 lower altitude (between 2400 and 2300 m asl, Middle Fracture, Fig. 1) along the SE flank of  
173 the summit cone and emitted most of the erupted volume (Figs. 2a and 2b). As often observed  
174 in PdF eruptions, the activity progressively focused on a narrow portion of the fractures at low  
175 altitude and finally on a single vent located at the lower tip of the fracture system (Main Vent,  
176 at 2336 m asl, Figs. 1, 2). The first in situ observations in the morning of June 21 (ca. 04h00  
177 GMT) showed that weak Strombolian activity was focused on a narrow segment of the lower  
178 fractures and that a'a lavas had already attained the elevation of 1983 m asl (0.2 km before  
179 maximum runout). A small, weak gas plume was also blowing northwards. A single sample of  
180 partially molten lava was collected from the still active lava front and partially water  
181 quenched. During most of June 21, the activity consisted of lava effusion in three parallel lava  
182 streams merging in a single lava flow and mild-weak "Strombolian" explosions at several  
183 closely spaced spots along the lower part of the feeding fracture. At 13.00 (GMT), only weak  
184 explosions were observed within a single small spatter cone (Figs. 2e and 2f). Most of the  
185 lava field was formed of open channel a'a lavas. The total volume of lava was estimated by  
186 MIROVA service (<https://www.sites.google.com/site/mirovaweb/home>), with the use of the  
187 MODIS images and the analyses of the flux from the spectral properties, to be within 0.34  
188 (+/- 0.12) million m<sup>3</sup>, (Coppola et al., 2017). Satellite derived volume estimates are consistent  
189 with independent photogrammetric estimates ( $0.4 \pm 0.2$  Mm<sup>3</sup>; Peltier et al., 2016) and rank the  
190 2014 eruption at the lower end of the volume range typically emitted by Piton de la Fournaise  
191 (Roult et al., 2012).

192 Apart from the sample from the front of the still active lava flow, all other samples  
193 were collected in two phases: 3 days after the eruption (pyroclasts on June 24, Fig. 3a; lavas  
194 on July 2) and three months later (pyroclasts from the Main Vent; November 18) (Table S1).  
195 June 24 samples were collected both from the main fractures, the Main Vent and the active  
196 lava flow (Fig. 1 and Table S1). Scattered scoriaceous bombs and lapilli were collected from  
197 the discontinuous deposits emplaced close to the Western Fracture, active only at the  
198 beginning of the eruptive event (Figs. 3c and 3d). In contrast, the sustained and slightly more



199 energetic activity at the lower tip of the fractures built a small spatter cone and accumulated a  
200 small volume of inversely graded scoria fallout. This deposit is 10 cm thick at 2 m from the  
201 vent and covers an area of about  $\sim 1000 \text{ m}^2$  (Main Vent, Fig. 1). For this fall deposit we  
202 collected two bulk samples, one from the base (within the lower 5 cm) and the other from the  
203 top (within the upper 5 cm), for the grain size and componentry analyses. The sample at the  
204 base was collected in November because on June 24 the loose proximal lapilli blanket was  
205 still very hot ( $405 \text{ }^\circ\text{C}$ ; thermocouple measurement, Fig. 3a) and fumaroles with outlet  
206 temperatures in the range  $305\text{-}60 \text{ }^\circ\text{C}$  were observed all along the fractures several weeks after  
207 the eruption. Both in June and in October, more than 200 clasts of similar size (maximum  
208 diameter between 16 and 32 mm, see Gurioli et al. 2015) were collected, both close to the  
209 Main Vent and in the ‘distal’ area (30 metres away from the vent) for density, connectivity,  
210 permeability, petrological and geochemical analysis.

211

### 212 3. Methodology

#### 213 3.1 Grain size, componentry and ash morphology

214 We performed grain size analyses on the two bulk samples collected from the Main Vent,  
215 following the procedure of Jordan et al. (2015) (Table S2). The samples were dried in the  
216 oven at  $90^\circ\text{C}$  and sieved at  $\frac{1}{2} \phi$  intervals in the range of  $-5 \phi$  to  $4 \phi$  (Fig. 3c); the data are  
217 also shown in full phi for comparison with the deposits of the 2010 PdF fountaining episode  
218 (Hibert et al., 2015; Fig. 3f). Sieving was carried out by hand and for not longer than three  
219 minutes to avoid breaking and abrasion of the very vesicular and fragile clasts. For the  
220 scattered scoria sampled from the Western Fracture (Figs. 1, 3c and 3d), we followed the grain  
221 size strategy proposed in Gurioli et al. (2013). Within this procedure we sampled each  
222 fragment and we recorded the weight and the three main axes (a being the largest, b, and c).  
223 To allow comparison with the sieving grain size analyses (Inman, 1952), we used the  
224 intermediate b axis dimension to obtain  $\phi = -\log_2 b$ .

225 Following the nomenclature of White and Houghton (2006) the componentry analysis is the  
226 subdivision of the sample into three broad components: i) juvenile, ii) non-juvenile particles,  
227 and iii) composite clasts. The juvenile components are vesicular or dense fragments, as well  
228 as crystals, that represent the primary magma involved in the eruption; non-juvenile material  
229 includes accessory and accidental fragments, as well as crystals that predate the eruption from  
230 which they are deposited. Finally, the composite clasts are mechanical mixtures of juvenile  
231 and non-juvenile (and/or recycled juvenile) clasts. In these mild basaltic explosions, the non-



232 juvenile component is very scarce, so we focused on the juvenile component that is  
233 characterized by three groups of scoria: (i) spiny-opaque, (ii) spiny-glassy, and (iii) fluidal,  
234 along with golden pumice (Fig. 4). The componentry quantification was performed for each  
235 grain size fraction between  $-5 \phi$  to  $0.5 \phi$  (Figs. 5a and 5b), where a binocular microscope was  
236 used for the identification of grains smaller than  $-1 \phi$  (Table S2). For the coarse ash fraction  
237 (250-300  $\mu\text{m}$  size) of the two bulk deposits collected at the Main Vent, we also performed a  
238 morphological quantification using the Morphologi G3 at Laboratoire Magmas et Volcans  
239 (LMV) of Clermont-Ferrand following the procedure of Leibbrandt and Le Pennec (2015) to  
240 distinguish between smooth versus spiny clasts within the coarse ash (Fig. 5c).

241 In the following, we will use the crystal nomenclature of Welch et al. (2009), with the  
242 strictly descriptive terms of macrocrysts ( $> 3$  mm in diameter) mesocrysts (from 0.3 to 3 mm  
243 in diameter), and microcrysts ( $< 0.3$  mm in diameter).

### 244 3.2 Particle bulk texture (density, porosity, connectivity) and microtexture

245 For each sample site, we selected 27 to 146 juvenile particles within the 8-32 mm fraction for  
246 density and pycnometry measurements (Table S3). This is the smallest granulometric fraction  
247 assumed to be still representative of the larger size class in terms of density (Houghton and  
248 Wilson, 1989; Gurioli et al., 2015), and has been used in previous textural studies (e.g., Shea  
249 et al., 2010). In addition, this size range is ideal for vesicle connectivity measurements (e.g.  
250 Formenti and Druitt, 2003; Giachetti et al., 2010; Shea et al., 2012; Colombier et al., 2017a,  
251 b). Textural measurements (density/porosity, connectivity) were performed at the LMV.  
252 Density of juvenile particles was measured by the water-immersion technique of Houghton  
253 and Wilson (1989), which is based on Archimedes principle. A mean value for the vesicle-free  
254 rock density was determined by powdering clasts of varying bulk densities, measuring the  
255 volumes of known masses using an Accupyc 1340 Helium Pycnometer, then averaging. The  
256 same pycnometer was also used to measure vesicle interconnectivity for each clast using the  
257 method of Formenti and Druitt (2003) and Colombier et al. (2017a). Vesicle size distribution  
258 and crystal content were performed following the method of Shea et al. (2010) on nine clasts  
259 picked up from each component-density distribution mode (Fig. 6c). These data are presented  
260 in Figure 4 and we followed the strategy of Leduc et al. (2015) for the quantification of the  
261 vesicle size distribution.

262 A full description of the protocol for density and connectivity measurements is  
263 available at <http://wwwobs.univ-bpclermont.fr/SO/televolc/dynvolc/index.php>, while the  
264 textural data are available at <http://wwwobs.univ-bpclermont.fr/SO/televolc/dynvolc/bdd.php>.





265

266 **3.3 Bulk geochemistry**

267 For the determination of the bulk chemistry (Table S4 and Fig. 7) of the different pyroclasts  
268 we selected the largest pyroclasts of golden pumice and the largest fluidal, spiny glassy and  
269 spiny opaque scoriae. We also analyzed two fragments of lava, from the beginning and the  
270 end of the eruption. Samples were crushed into coarse chips using a steel jaw crusher and  
271 powdered with an agate mortar. Major and trace element compositions were analyzed using  
272 powder (whole rock composition). In addition, for a sub-set of pyroclasts, glass chips (2-5  
273 mm in size) were hand-picked under a binocular microscope and analyzed separately for trace  
274 elements. For major element analysis, powdered samples were mixed with LiBO<sub>2</sub>, placed in a  
275 graphite crucible and melted in an induction oven at 1050 °C for 4.5 minutes, resulting in a  
276 homogeneous glass bead. The glass was then dissolved in a solution of deionized water and  
277 nitric acid (HNO<sub>3</sub>), and finally diluted by a factor of 2000. The final solutions were analyzed  
278 by ICP-AES. Trace element concentrations were analysed following a method modified from  
279 Vlastelic et al. (2013). About 100 mg of sample (powder and chip) were dissolved in 2 ml of  
280 28M HF and 1 ml of 14M HNO<sub>3</sub> in teflon beaker for 36 hours at 70°C. Solutions were  
281 evaporated to dryness at 70°C. The fluoride residues were reduced by repeatedly adding and  
282 evaporating a few drops of concentrated HNO<sub>3</sub>, before being fully dissolved in ca. 20 ml of  
283 7M HNO<sub>3</sub>. These solutions were diluted by a factor of 15 with 0.05M HF (to reach rock  
284 dilution factor of ca. 4000) and trace element abundances were determined by quadrupole  
285 ICPMS (Agilent 7500). The analyses were performed in plasma robust mode (1550 W). The  
286 reaction cell (He mode) was used to reduce interference on masses ranging from 45 (Sc) to 75  
287 (As). The signal was calibrated externally (every 4 samples) with a reference basaltic standard  
288 (USGS BHVO-2) dissolved as for the samples and using the GeoRem recommended values  
289 (<http://georem.mpch-mainz.gwdg.de/>). For elements that are not well characterized in  
290 literature (As, Bi, Tl), or which show evident heterogeneity (e.g. Pb) in BHVO-2 powder, the  
291 signal was calibrated using the certified concentrations of a synthetic standard, which was  
292 also repeatedly measured. The external reproducibility (2σ error) of the method is 6% or less  
293 for lithophile elements and 15% or less for chalcophile elements.

294

295 **3.4 Glass and crystal chemistry**

296 Spot analyses of matrix glass and crystal composition (Table S5) were carried out using a  
297 Cameca SX100 electron microprobe (LMV), with a 15 kV acceleration voltage of 4 nA beam



298 current and a beam of 5  $\mu\text{m}$  diameter for glass analyses. However, for the spiny opaque  
299 scoria, characterized by abundant crystals with rapid growth textures, a voltage of 8 nA beam  
300 current and a beam of 10  $\mu\text{m}$  diameter were used. For this latter sample, 10 analyses per  
301 sample were performed due to the heterogeneity within the highly crystallised glass (Fig. 8a),  
302 while for the other samples 6 analyses per sample were enough to characterize the clean  
303 homogeneous glass. For crystal analysis, a focused beam was used. For the characterization of  
304 the meso- and micro-crysts, due to their small size, only two measurements were performed,  
305 one at the edge and one at the core of the crystals, to check for possible zonation.

306

### 307 **3.5 Melt inclusions**

308 Melt inclusions (MIs; Table S6, Figs. 8b and 9) were characterized in the olivine mesocrysts  
309 from the three groups of scoriae (fluidal, spiny glassy and spiny opaque). Crystals in the  
310 pumice group were too rare and small to be studied for melt inclusions.

311 Olivine crystals were handpicked under a binocular microscope from the 100– 250 and  
312 250– 600  $\mu\text{m}$  grain size fractions of crushed tephra. Crystals with MIs were washed with  
313 acetone, embedded in epoxy and polished individually to generate adequate exposure of the  
314 MIs for *in situ* electron probe microanalysis. The MIs are spherical to oblate in shape and  
315 range in size from 10 to 200  $\mu\text{m}$ . Some of the MIs contain shrinkage bubbles but all of those  
316 studied are totally deprived of daughter minerals. Major elements were measured on a  
317 Cameca SX-100 microprobe at LMV (Table S6). For major elements, the larger MIs were  
318 analyzed with a spot diameter of 10-20  $\mu\text{m}$  and sample current of 8 nA, whereas the smaller  
319 MIs were analyzed with a beam of 5  $\mu\text{m}$  and a sample current of 4 nA. The results are given  
320 in Table S6, and analytical details and uncertainties are listed in Óladóttir et al. (2011) and  
321 Moune et al. (2012).

322

## 323 **4 Results**

### 324 **4.1 Deposit texture (grain size, componentry, morphology) and petrological description** 325 **of the samples**

326 The pyroclastic deposits at the Western and Upper fractures sites (Fig. 1a) are formed by  
327 scattered homogeneous smooth fluidal (Figs. 3d) bombs and lapilli. The average dimension of  
328 the fragments is around 4 cm (maximum axis) with bombs up to 10 cm and scoria lapilli up to  
329 2 cm in size.



330 At the Main Vent, the reversely graded deposit is made up of lapilli and bombs, with  
331 only minor coarse ash (Fig. 3c). The lower 5 cm at the base are very well-sorted and show a  
332 perfect Gaussian distribution with a mode at 4 mm. In contrast, the grain size distribution of  
333 the upper 5 centimetres is asymmetrical with a main mode coarser than 22 cm and a second  
334 mode at 8 mm. This upper deposit is negatively skewed due to the abundance of coarse clasts.  
335 The dataset show a similarity between the grain size distributions of the basal tephra ejected  
336 from the 2014 main vent and the ones for the lava fountaining of the 2010 summit event  
337 (Hibert et al., 2015). On the contrary, the top of the 2014 fall differs from fountain deposits,  
338 being coarser and polymodal, and it is ascribed to dominantly Strombolian activity.

339 In terms of componentry of the deposits, four types of clasts were distinguished (Fig.  
340 4): (i) golden pumice, (ii) smooth or rough fluidal scoriae, (iii) spiny glassy scoria, (iv) spiny  
341 opaque scoria. The pumices are vesicular, light fragments, characterized by a golden to light  
342 brown color, sometimes with a shiny outer surface (Fig. 4a). They are usually rounded in  
343 shape. Golden clasts studied for textures contain a few microcrysts of plagioclase (up to 0.1  
344 mm in diameter), clinopyroxene up to 0.05-0.06 mm in diameter, and small olivine up to 0.03  
345 mm in diameter (Fig. 4), together with large areas of clean, light brown glass. The fluidal  
346 scoria fragments have dark, smooth or rough shiny surfaces (Fig. 4b). They can be more or  
347 less elongated in shape and have spindle as well as flattened shapes. The fluidal fragments are  
348 characterized by rare mesocrysts of plagioclase and clinopyroxene and microcrysts of  
349 plagioclase, clinopyroxene and olivine (Fig. 4b). The spiny glassy fragments are dark, spiny  
350 scoria that range in shape from subrounded to angular (Fig. 4c). These fragments contain  
351 abundant glassy areas, while the spiny opaque fragments lack a glassy, iridescent surface.  
352 Both groups of spiny clasts are characterized by the presence of dark and light brown glass.  
353 The spiny opaque fragments are the densest fragments and have the largest amount of  
354 crystals. They contain, as the most abundant phase, relatively large meso- and micro-crysts of  
355 plagioclase, up to 3 mm long, together with meso- and micro-crysts of clinopyroxene and  
356 olivine (Figs. 4c and 4d). In the dark portions of their matrix, tiny fibrous microcrysts of  
357 olivine + clinopyroxene + plagioclase + Fe-Ti oxides occur. The spiny glassy fragments have  
358 the same crystal populations as the spiny opaque ones, but their plagioclases are much smaller  
359 and attain a maximum length of only 0.3 mm. Clusters of plagioclase and clinopyroxene are  
360 present in both the spiny opaque and the spiny glassy fragments, as well as rare macrocrysts  
361 of olivine. The olivine macrocrysts exhibit the typical compositional (Fo 84.2) and  
362 petrographic features of olivine phenocrysts described in previous studies (Clocchiatti et al.,  
363 1979; Albarede and Tamagnan, 1988; Bureau et al., 1998a and b; Famin et al., 2009; Welsch



364 et al., 2013). They are automorphic, fractured with oxides (mostly chromite) and melt  
365 inclusions (Fig. 4c). Fluidal and pumice fragments studied for textures contain rare  
366 macrocrysts and mesocrysts of olivine, and the crystals are essentially microlites. The pumice  
367 and some fluidal fragments have lower contents of microlites than some fluidal and spiny  
368 fragments, with the latter having the highest microlite content (Table S4).

369 The componentry results are reported in Figure 5 for the Main Vent deposits; the  
370 deposits from the Fractures are characterized exclusively by fluidal clasts (Fig. 3). At the base  
371 of the Main Vent deposit, the coarse fraction of the deposit is rich in golden and fluidal  
372 components that represent more than 60-70vol% (Figs. 5a and 5b). The proportion of the two  
373 groups is similar. If we look at the Morphologi G3 results (Fig. 5c) for the coarse ash  
374 fragments, this population is formed exclusively by smooth fragments that correspond to  
375 fluidal and golden pumice. In contrast, in the upper, coarse grained fall deposit, the clasts  
376 bigger than 8 mm are dominated by the spiny scoria fragments, while the fraction smaller than  
377 8 mm show a dramatic increase in the golden and fluidal fragments, with the fluidal ones  
378 always more abundant than the golden ones (Figs. 5a and 5b). The small amount of coarse ash  
379 fraction in the top deposit, however, is dominated by the presence of spiny fragments (Fig.  
380 5c). Abundant light, golden, coarse lapilli pumice and bombs have been found scattered  
381 laterally up to 30 metres from the main axis and were not found in the proximal deposit. On  
382 the basis of the high amount of pumice in the lower part of the deposit, we correlate the large,  
383 light clasts with the base of the proximal deposit, and consequently we interpret them as  
384 material emitted at the beginning of the June 2014 eruptive event.

385

#### 386 4.2 Particle density, porosity connectivity and texture

387 Density analyses performed on 200 coarse lapilli (Table S3) reveal a bimodal distribution,  
388 with a main population of light fragments having a mode at  $800 \text{ kg/m}^3$ , and a second and  
389 denser population centered at  $1400 \text{ kg/m}^3$  (Fig. 6a). The fluidal fragments, mostly collected at  
390 the Western Fracture (Fig. 1a), have a density range from 600 to  $1400 \text{ kg/m}^3$  and a mode at  
391  $1000 \text{ kg/m}^3$  (Fig. 6b). The bulk deposit collected close to the Main Vent has a bimodal  
392 density distribution, with the golden and fluidal fragments forming the lower-density  
393 population and the spiny fragments being dominant in the denser population (Fig. 6c). For  
394 these samples there is a marked correlation between porosity and morphology, so that the  
395 spiny-opaque clasts are the densest (up to  $1600 \text{ kg m}^{-3}$ , with a vesicularity of 45 vol%) and the  
396 golden pumice are the lightest (minimum density of  $400 \text{ kg m}^{-3}$  with a vesicularity of up to 86



397 vol%; with a Dense Rock Equivalent density of  $2.88 \times 10^3 \text{ kg m}^{-3}$ ). The increase in  
398 vesicularity correlates with an increase in the amount of small (0.1 mm), medium (0.5-1 mm)  
399 and large (up to 4 mm) vesicles. In the fluidal clasts, these vesicles have a regular rounded or  
400 elliptical shape and are scattered throughout the sample. The lightest pumices are often  
401 characterized by the presence of a single, large central vesicle (10 – 15 mm) with the little  
402 vesicles and a few medium vesicles distributed all around it (Fig. 4). The spiny glass texture is  
403 characterized by a lower amount of large vesicles than in the pumice and by the presence of  
404 mostly medium sized vesicles, while the spiny opaque has more irregular shaped, very large  
405 (up to 10 mm) vesicles with a small and a medium sized bubble population. In the spiny glass  
406 samples, the glass is more or less brown, with the dark brown portions being the ones with the  
407 lowest vesicle content and the highest microlite content. The opaque samples have a central,  
408 very dark glass portion, with low vesicle content, and a more vesicular glassy portion at the  
409 outer edges (Fig. 4).

410 The connectivity data (Fig. 6d) also indicate that the fluidal and golden clasts have a  
411 larger amount of isolated vesicles (up to 40% in volume). The fluidal clasts from the Western  
412 Fracture are the most homogeneous with an average percentage of isolated vesicles around  
413 30% in volume. Both the pumice and the fluidal fragments with high vesicularity are  
414 characterized by fewer amounts of isolated vesicles. Finally the spiny fragments have the  
415 lowest content of isolated vesicles (0-5% in volume).

416

#### 417 **4.3 Chemistry and geochemistry of the products**

418 Major and trace element concentrations of whole-rock and hand-picked glass samples are  
419 reported in Table S4. Whole rock major element composition is very uniform (e.g.,  
420  $6.5 < \text{MgO} < 6.7 \text{ wt\%}$ ) and well within the range of Steady State Basalts (SSB), the most  
421 common type of basalts erupted at Piton de la Fournaise (Albarède et al., 1997). However,  
422 compatible trace elements, such as Ni and Cr, are at the lower end of the concentration range  
423 for SSB ( $< 100 \text{ ppm}$ ) indicating that the June 2014 eruption sampled relatively evolved melts.  
424 Ni and Cr generally show higher concentrations in 2014 bulk rocks ( $79 < \text{Ni} < 92 \text{ ppm}$  and  
425  $71 < \text{Cr} < 87 \text{ ppm}$ ) compared to the 2014 glass chips ( $66 < \text{Ni} < 73 \text{ ppm}$  and  $54 < \text{Cr} < 59 \text{ ppm}$  for all  
426 but two chips). In the Cr vs Ni plot (Fig. 7a), whole rocks plot to the right of the main  
427 clinopyroxene +/- plagioclase-controlled melt differentiation trend. This trend is controlled by  
428 the addition of Ni-rich olivine (Albarède and Tamagnan, 1988). We estimate that the Ni  
429 excess results from the occurrence of a low amount (0.7 to 1.3 wt%) of cumulative olivine in



430 whole rocks, consistent with thin section observations. The composition of olivine  
431 macrocrysts (ca. Fo<sub>84</sub>) is too magnesian to be in equilibrium with the low-MgO evolved  
432 composition of the 2014 magma. Using our estimate for the amount of cumulative olivine, we  
433 recalculate the olivine-corrected MgO content of the 2014 magma at 6.2 wt%. The June 2014  
434 melt is thus only moderately depleted in compatible elements compared to the previous  
435 eruption of December 2010 (MgO~6.6 wt%, Ni~80 ppm, Cr~120 ppm). Conversely, the June  
436 2014 melt is significantly depleted in compatible elements compared to the earlier November  
437 2009 eruption, which sampled relatively primitive magmas (average MgO~7.7 wt%, Ni~135  
438 ppm, Cr~350 ppm) (Fig. 7a). The 2014 evolved composition plots at the low-Ni-Cr end of  
439 Piton de la Fournaise historical differentiation trend (Albarède and Tamagnan, 1988), near the  
440 composition of lavas erupted on 9 March 1998 after 5.5 years of quiescence (1992-1998).  
441 Note that olivine accumulation at PdF generally occurs in melt having ca.100 ppm Ni  
442 (Albarède and Tamagnan, 1988). Olivine accumulation in evolved melts (Ni < 70 ppm) seems  
443 to be a distinctive feature of many small post-2007 eruptions (e.g. this event and the three  
444 2008 eruptions, see Di Muro et al., 2015).

445 A closer inspection of Ni-Cr variability in June 2014 whole rock samples (Fig. 7b) reveals  
446 that scoria from the Western Fracture (140624-9b-6, Table S4) and early erupted lavas (1406-  
447 21-1, Table S4) have the lowest amount of olivine (<0.9%) whereas scoria from the Upper  
448 Fracture (140624-13a) and late erupted lavas (140324-12) have a slightly higher amount of  
449 olivine (>1.2%). This is consistent with the general trends observed at PdF of olivine increase  
450 from the start to end of an eruption (Peltier et al., 2009).

451 The so called “olivine control trend” in Ni-Cr space cannot be explained either by addition of  
452 pure olivine (which contains less than 500 ppm Cr (Salaün et al., 2010; Di Muro et al., 2015;  
453 Welsch et al., 2009), or by the addition of olivine plus pyroxene (which would require ca.  
454 50% pyroxene with 970 ppm Ni and 4800 ppm Cr, see Fig. 7 caption). Instead, addition of  
455 olivine hosting ca. 1% Cr-spinel (with 25 wt.% Cr) accounts for data and observations, and is  
456 consistent with crystallization of olivine and Cr-spinel in cotectic proportions (Roeder et al.,  
457 2006). The fact that some samples (golden pumice) plot off the main, well-defined array, can  
458 be explained either by addition of more or less evolved olivine crystals (with the range of Fo  
459 80-85 measured in June 2014 samples) and/or slight variations ( $\pm 0.02\%$ ) in the proportion of  
460 Cr-spinels (Fig. 7b).

461 The glass chemistry of the four clast types allows us to correlate porosity and oxide  
462 contents and shows an increase in MgO from the spiny opaque to fluidal and golden  
463 fragments (Fig. 8a). Consistent with petrological and textural observations, the spiny opaque



464 is the most heterogeneous type of clast in terms of glass composition (Fig. 8). The glassy  
465 portion at the edge of the clast is similar to the spiny glass, while the interior, characterized by  
466 dark areas rich in tiny fibrous microcrysts, shows scattered glass compositions with very low  
467 MgO content as well as a decrease in CaO (Fig. 8). We attribute the significant variation in  
468 glass composition within the different components to variable degrees of micro-crystallisation  
469 as the bulk chemistry of all clasts is very similar and globally homogeneous.

470

#### 471 4.4 Melt inclusions

472 MI analyses must be corrected for post-entrapment host crystallisation at the MI - crystal  
473 interface. We used a  $K_d = (\text{FeO}/\text{MgO})_{\text{ol}} / (\text{FeO}/\text{MgO})_{\text{melt}} = 0.306$  (Fisk et al., 1988; Brugier,  
474 2016) and an average  $\text{Fe}^{3+}/\Sigma\text{Fe}_{\text{total}}$  ratio of 0.11 (Bureau et al., 1998a; Di Muro et al., 2016 and  
475 references therein) defined for PdF magmas. For the June 2014 melt inclusions, the post  
476 entrapment crystallization (PEC) ranges from 2.9 to 10.5 wt%. Raw and corrected major and  
477 volatile element concentrations of MIs are reported in Table S6.

478 Host olivines span a large compositional range from Fo<sub>80</sub> to Fo<sub>86</sub>. Despite the evolved  
479 bulk composition of the magma, most olivines are quite magnesian (Fo<sub>83-85</sub>) and are not in  
480 equilibrium with the evolved host magma. On the contrary, Mg-poor olivines (Fo<sub>80-81</sub>) can be  
481 considered as being in equilibrium with the bulk rock composition. The corrected  
482 compositions of MIs in phenocrysts from the different samples partly overlap with the  
483 evolved bulk rocks (MgO<sub>wr</sub>: 6.1-7.2 wt%) and extend to higher MgO contents of up to 8.8  
484 wt% (Table S6). MIs display a narrow range of transitional basaltic compositions (K<sub>2</sub>O= 0.5-  
485 0.9 wt%) and show no significant difference between the three types of scoriae. The major  
486 element composition of melt inclusions correlates with that of the host olivines. Melt  
487 inclusions in the high Fo-olivines have the highest MgO, CaO and TiO<sub>2</sub> and lowest K<sub>2</sub>O  
488 concentrations (Table S6). It is interesting to note that the June 2014 products contain two  
489 populations of magnesian (Fo<sub>>83</sub>) olivines hosting melt inclusions with two distinct Ca  
490 contents. Most of the magnesian olivines contain MIs with unusually high CaO contents (11.6  
491 – 12.9 wt%) and high CaO/Al<sub>2</sub>O<sub>3</sub> ratios (0.8-0.9), higher than that of the bulk rocks (0.8) (Fig  
492 8). The occurrence of olivines with “high Ca” melt inclusions has been observed in all three  
493 different types of scoriae. A few magnesian olivines and all Mg-poor olivines (Fo<sub>80.5-83.6</sub>) host  
494 MIs with lower CaO contents (11.4 wt%). This latter composition overlaps with that of the  
495 bulk rock (Fig 8). The “high Ca” population of inclusions is also enriched in TiO<sub>2</sub> and Al<sub>2</sub>O<sub>3</sub>  
496 and depleted in MgO, FeO<sub>T</sub> and Na<sub>2</sub>O for a given olivine Fo content with respect to the “low



497 Ca” population. Both low- and high-Ca populations of melt inclusions have similar K<sub>2</sub>O  
498 contents and total alkali content increases from 3 wt% at 12.6 wt% CaO, to 3.5 wt% at 10.8  
499 wt% CaO. However, we remark that high Ca melt inclusions from the June 2014 activity  
500 record a significant scattering in K<sub>2</sub>O contents, which range from 0.55 to 0.9 wt%.

501 MIs in olivines from June 2014 can best be compared with those of other recent small-  
502 volume and short-lived eruptions which emitted basalts with low phenocryst contents, like  
503 those in March 2007 (0.6 Mm<sup>3</sup>) and November 2009 (0.1 Mm<sup>3</sup>) (Roult et al., 2012). March  
504 2007 aphyric basalt has a bulk homogeneous composition with intermediate MgO content  
505 (MgO<sub>wr</sub>: 7.33 wt%; K<sub>2</sub>O: 0.67 wt%). Their olivines (Fo 81) are in equilibrium with the bulk  
506 rock and their composition is unimodal (Di Muro et al., 2014). November 2009 products are  
507 the most magnesian lavas emitted in the 2008-2014 period, slightly zoned (MgO<sub>wr</sub>: 7.6-8.3  
508 wt%; K<sub>2</sub>O: 0.75 – 0.62 wt%) and contain a few percent of normally zoned olivine macrocrysts  
509 with bimodal composition (Fo<sub>81</sub> and Fo<sub>83.5</sub>, see Di Muro et al., 2016). June 2014 bulk rocks  
510 (MgO<sub>wr</sub>: 6.7 wt%; K<sub>2</sub>O: 0.75 wt%) and melt inclusions in Fo<sub>80-81</sub> olivines are quite evolved.  
511 Their composition is close to that of products emitted by summit intracaldera eruptions in  
512 2008, ca. 1.5 years after the large 2007 caldera forming eruption (Di Muro et al., 2015) (Fig.  
513 8). As already reported for 2008 products, many olivine macrocrysts of 2014 are clearly too  
514 magnesian to be in equilibrium with the relatively evolved host melts. Overall, MgO content  
515 in 2007-2014 melt inclusions tends to decrease with decreasing Fo content of the host  
516 olivines. MIs in olivines also exhibit a trend of linear decrease in MgO and increase in FeO  
517 from April 2007 to 2009-2014 products (Fig. 9). Melt inclusions in March 2007, November  
518 2009 and June 2014 follow the same trend of FeO enrichment (Fig. 9). In the large-volume  
519 and olivine-rich April 2007 products, MIs in magnesian olivines with Fo<sub>>82</sub> have distinctly  
520 higher MgO, FeO and lower SiO<sub>2</sub> and Al<sub>2</sub>O<sub>3</sub> than MIs in 2009-2014 products. The distinctive  
521 FeO enrichment of many of the MIs from the April 2007 oceanite has been interpreted by Di  
522 Muro et al. (2014) as a result of post-entrapment modification during long lasting magma  
523 storage.

524 Two populations of low- and high-Ca melt inclusions are also found in the November  
525 2009 olivines. Low-Ca melt inclusions from the November 2009 and June 2014 eruptions  
526 indicate a single trend of chemical evolution (Fig. 8), consistent with bulk rock compositions.  
527 June 2014 products have lower MgO and CaO contents than those from November 2009.  
528 Significant scattering in K<sub>2</sub>O content (0.6-0.9 wt%) is found in low-Ca inclusions from 2009,  
529 as observed in high-Ca inclusions from the 2014 eruption, but they share similar K<sub>2</sub>O  
530 contents. In 2009 and 2014 products, K<sub>2</sub>O content of melt inclusions is partly anti-correlated





531 with the olivine Fo content. This observation has been attributed to moderate heterogeneity of  
532 primary melts feeding the plumbing system of PdF. Rapid temporal changes of K<sub>2</sub>O content in  
533 PdF basalts have been reported (Boivin and Bachelery, 2009).

534

#### 535 **4.5 Mineral composition and glass – plagioclase equilibrium**

536 All 2014 scoriae (spiny, fluidal, golden) contain the same paragenesis of olivine,  
537 clinopyroxene and plagioclase. The composition of minerals found in golden, fluidal and  
538 spiny scoriae is indistinguishable.

539 In olivines, average MgO content decreases from macrocrysts (Fo<sub>84.1</sub>) to mesocrysts  
540 (Fo<sub>79.6</sub>) to microlites. Olivine microlites (Table S5) are normally zoned. Their composition  
541 ranges from Fo<sub>78.0-75.3</sub> in the cores to Fo<sub>74.3-70.5</sub> in the rims. Overall, olivines in 2014 products  
542 span the full range of typical Fo contents of recent Piton de la Fournaise magmas (Boivin and  
543 Bachelery, 2009; Di Muro et al., 2014; 2015). Clinopyroxene composition (augites) ranges  
544 from En<sub>53</sub>Fs<sub>15</sub>Wo<sub>32</sub> to En<sub>41</sub>Fs<sub>14</sub>Wo<sub>45</sub>. Their average composition (En<sub>45</sub>Fs<sub>14</sub>Wo<sub>41</sub>) is consistent  
545 with that found in other recent evolved melts like those emitted by the 2008 eruptions (Di  
546 Muro et al., 2015) and more generally in recent Piton de la Fournaise products (Boivin and  
547 Bachelery, 2009). Clinopyroxenes are unzoned, the composition of cores and rims is very  
548 similar and close to that found in microcrysts and mesocrysts. Plagioclase composition ranges  
549 from An<sub>79.5</sub>Ab<sub>19.9</sub>Or<sub>0.6</sub> to An<sub>63.1</sub>Ab<sub>35.7</sub>Or<sub>1.2</sub> with a bimodal distribution (An<sub>76.5-79.5</sub> and An<sub>63.1-</sub>  
550 <sub>72.9</sub>). Similar bimodal distribution was observed in the evolved 2008 products, in particular  
551 from the November 2008 eruption (Di Muro et al., 2015). Mesocrysts (An<sub>75.5</sub>Ab<sub>23.8</sub>Or<sub>0.7</sub> on  
552 average) are more calcic with respect to microcrysts (An<sub>65.7</sub>Ab<sub>33.1</sub>Or<sub>1.2</sub> on average). Normal  
553 zoning is commonly found from plagioclase cores to rims, which contrasts with the complex  
554 zoning patterns previously reported for the 2008 products (Di Muro et al., 2015).

555 Plagioclase-melt equilibrium and melt composition in pyroclastic rocks and water-  
556 quenched lavas were used to estimate both temperature and water content dissolved within the  
557 melt (Table S5). Temperature estimates are based on the equation of Helz and Thornber  
558 (1987) modified by Putirka (2008). Water content was calculated from the plagioclase  
559 hygrometer of Lange et al. (2009) at 50 MPa corresponding to the maximum CO<sub>2</sub>-H<sub>2</sub>O  
560 pressure estimation (recalculated with Papale et al., 2006), typically recorded in melt  
561 inclusions from central products at PdF (e.g. 1931 eruption; (Di Muro et al., 2016) and  
562 references therein). This pressure roughly corresponds to the sea level depth, which is inferred  
563 to be the location of the potential main shallow magmatic reservoir (Peltier et al., 2009;



564 Lengliné et al., 2016; Coppola et al., 2017). The application of the hydrous thermometer of  
565 Putirka (2008) makes it possible to estimate the dissolved water content in the melt with a  
566 nominal uncertainty of 0.15 wt% and is only slightly dependent on pressure. Plagioclase  
567 compositions not in equilibrium with the melt (glass or bulk rock) are those mesocryst cores  
568 with the highest ( $An_{>76.5}$ ) anorthite content (Table S5). Such compositions are more in  
569 equilibrium with CaO-richer magnesian melts than those measured in matrix glasses and bulk  
570 rocks of 2014 eruption.

571 In order to determine pre-eruptive conditions, calculations were performed only on  
572 paired plagioclase rims and matrix glasses in equilibrium, using the plagioclase-melt  
573 equilibrium constant of Putirka (2008) calibrated for melts whose temperature exceeds  
574 1050°C ( $K_{d_{An-Ab}} = 0.27 \pm 0.05$ ). Our review of published and unpublished data shows that melt  
575 temperature progressively decreases from April 2007 (1188 $\pm$ 16 °C) to January-October  
576 2010 (1147 $\pm$ 9°C) and positively correlates with K<sub>2</sub>O content in melts which increases from  
577 0.70 to 0.96 wt% (Fig. 10). The melts from the June 2014 eruption record the lowest  
578 temperatures in post-2007 eruptions (1131 $\pm$ 15 °C) together with the highest K<sub>2</sub>O-enrichment  
579 (K<sub>2</sub>O: 0.90 $\pm$ 0.12 wt%). The lowest temperatures are recorded by spiny scoriae, while the  
580 temperature of golden scoriae overlaps with that of 2010 products emitted before the 2010-  
581 2014 phase of quiescence. In spite of the large variability in melt composition and  
582 temperature, average pre-eruptive water content dissolved in the melts (0.5  $\pm$  0.2 wt%) is  
583 quite homogeneous for the whole 2008-2014 period. In 2014, the lowest estimated dissolved  
584 water content (down to 0.38 wt%) is for the golden and some fluidal scoriae, while the  
585 maximum amount (0.68 wt%) is for the spiny opaque scoriae. However, water content  
586 estimated from core-bulk rock equilibrium (0.3 $\pm$ 0.1 wt%) is slightly lower than that estimated  
587 from rim and microlite-matrix glass equilibrium (0.5 $\pm$ 0.2 wt%), but the difference broadly  
588 overlaps the nominal uncertainty related to calculations. Dissolved water contents in melts of  
589 the pyroclasts are thus lower than those measured in 2007 melt inclusions (H<sub>2</sub>O: 0.8  $\pm$  0.15  
590 wt% and up to 1.1 wt%) and higher than typically found in degassing matrices of lava and  
591 Pele's hairs of 2007 (Fig. 10; 0.2 wt%; see Di Muro et al., 2015; 2016).

592

## 593 **5 Discussions**

### 594 **5.1 The activity**

595 The activity fed by the uppermost Western Fractures (Fig. 1) was very short-lived, as shown  
596 by the presence of only scattered bombs and coarse lapilli (Fig.s 3c and 3d). The homogeneity



597 of these clasts, their coarse grained nature and the fluidal smooth texture are in agreement  
598 with very short-lived fire-fountaining/magma jets. Glassy outer surfaces of clasts have been  
599 interpreted as a late-stage product of fusion by hot gases streaming past the ejecta within the  
600 jet/fountain (Thordarson *et al.*, 1996; Stovall *et al.*, 2011). However, the occurrence of this  
601 process is not supported by the homogeneous glass composition in our fluidal clasts.

602 At lower altitude and close to the Main Vent (Fig. 1), the 5 cm layer at the base of the  
603 fall deposit is fine-grained (Fig. 3b), rich in fluidal and golden fragments, with a perfect  
604 Gaussian grain size curve (Fig. 5), and similar to that reported from the weak 2010  
605 fountaining event (Fig. 3e and Hibert *et al.*, 2015). Therefore we interpret this deposit as being  
606 due to weak Hawaiian like fountaining (sustained, but short-lived) activity. The top of the  
607 same deposit is coarse grained, bimodal, has a lower content in coarse ash (Table S2) and is  
608 rich in spiny opaque and spiny glass fragments. The reverse grain size likely records the  
609 transition from early continuous fountaining to late discrete Strombolian activity, typical of  
610 many eruptions at PdF (Figs. 2a and 2b and Hibert *et al.*, 2015). The reverse grading of the  
611 whole deposit (Fig. 3b) is thus not correlated with an increase in energy of the event, but with  
612 two different eruptive dynamics and fragmentation processes. The decrease in coarse ash,  
613 which correlates with the decrease in energy of the event, highlights the most efficient  
614 fragmentation process within the Hawaiian fountaining with respect to the slow gas ascent  
615 and explosion of the Strombolian activity. These conclusions are consistent with (i) the  
616 continuous and progressive decrease in intensity of Real time Seismic Amplitude  
617 Measurement recorded by the OVPF seismic network (unpublished data), and (ii) satellite  
618 derived TADR (Coppola *et al.*, 2017) which suggest continuous decay of magma output rate  
619 after an initial short-lived intense phase.

620

## 621 **5.2 Interpretation of the different textural signatures and the meaning of the 4 typologies** 622 **of clasts.**

623 The first microtextural analysis of Hawaiian ejecta was performed by Cashman and Mangan  
624 (1994) and Mangan and Cashman (1996) on pyroclasts from 1984 to 1986 Pu‘u ‘Ō‘ō  
625 fountainings. The authors defined two clast types: 1) ‘scoria’ consisting of closed-cell foam of  
626  $\leq 85\%$  vesicularity, with round, undeformed, broadly-sized vesicles, and 2) ‘reticulite’, an  
627 open-cell polyhedral foam with  $\sim 1 \mu\text{m}$  thick vesicle walls with  $>95\%$  vesicularity. They stated  
628 that the scoria to reticulite transition is a consequence of Ostwald ripening, where larger  
629 bubbles grow at the expense of smaller bubbles due to post-fragmentation expansion of clasts



630 within the fountain. According to this model, scoria preserves textures closer to conditions at  
631 fragmentation, whereas continued vesiculation and clast expansion in the thermally-insulated  
632 core of the fountain results in reticulate. This model was confirmed at lava fountains at Etna  
633 (Polacci et al., 2006), Villarrica (Gurioli et al., 2008), Kīlauea Iki, (Stovall et al., 2011 and  
634 2012), Mauna Ulu (Parcheta et al., 2013) and Al Madinah (Kawabata et al., 2015). These last  
635 authors also measured the connected and isolated porosity in the AD1256 Al-Madinah  
636 Hawaiian fountaining eruptions. They found that the reticulite-like textures from the central  
637 part of these very high fountains showed isolated vesicles in agreement with low shear rates  
638 and low viscosity melts, where bubbles may grow spherically and remain isolated. In contrast,  
639 at margins of the fountains, high shear may lead to stretching and mechanical coalescence of  
640 bubbles, forming the common, fluidal types of particles seen also in the deposits. They also  
641 stated that lower vesicularity and greater isolated porosity were found in some tephra  
642 interpreted as resulting from Strombolian eruptive phases.

643 The data that we found in our study of the typical activity of PdF agree only partially  
644 with all these interpretations. The reason is that we sampled and measured products of very  
645 weak Hawaiian to Strombolian activities. If we plot the approximate durations and masses of  
646 these events on the Houghton et al. (2016) diagram, the 2014 activity of PdF falls into the two  
647 fields for transient and fountaining activity, but at the base of the diagram. We here show for  
648 the first time that short lived and weak fountaining can preserve pyroclast textures that can be  
649 considered as representing a valid approximation to magma ascent and fragmentation  
650 conditions before the explosions. The occurrence of time-variable ascent conditions is also  
651 reflected in the time evolution of explosion dynamics, with the golden and fluidal emitted  
652 from the low fountaining episodes and the spiny fragments from the Strombolian-like  
653 explosions. This is quite evident when, following Stovall et al. (2011), we use a plot of  
654 vesicle-to-melt ratio ( $V_g/V_l$ , after Gardner et al., 1996) and vesicle number density ( $N_v$ ). As  
655 explained by Stovall et al. (2011), addition of small bubbles leads to an increase in  $N_v$  and  
656 only a slight increase in  $V_g/V_l$ . Bubble growth by some combination of diffusion and  
657 decompression leads to an increase in  $V_g/V_l$  at constant  $N_v$ .  $N_v$  decreases while  $V_g/V_l$   
658 increases during bubble coalescence, whereas loss of bubbles via collapse or buoyant rise  
659 leads to a reduction in both parameters. Intermediate trends on the diagram reflect  
660 combinations of more than one of these processes. The pumice and the scoria from the Main  
661 Vent of PdF show the highest  $V_g/V_l$ , but also the highest  $N_v$ , suggesting preservation of small  
662 vesicles and growth by some combination of diffusion and decompression. The presence of  
663 the small vesicles confirms that the weak PdF activity leads to only limited post-



664 fragmentation expansion inside the hot portions of the short-lived fountains. These data  
665 contrast with the data from the more energetic fountaining events observed at Kilauea or  
666 elsewhere, where pre-eruptive information is basically erased because pumice textures are  
667 dominated by expansion effects due to their longer permanence within the long-lived  
668 fountaining. In contrast, the densest, spiny scoriae and the scoria from the Fractures activity  
669 show the lowest values of  $N_v$  and  $V_g/V_l$ , due to incipient coalescence and/or loose/lack of  
670 small bubbles.

671         The golden and fluidal fragments, from the Main Vent, show the highest vesicularity,  
672 variable proportions of isolated vesicles and high, but variable,  $N_v$  numbers (Figs. 4, 6d and  
673 11). They are also characterized by a uniform vesicle population with clear evidence of  
674 incipient expansion (Fig. 4). From the connectivity graph, there is a clear decrease in isolated  
675 vesicles with the increase in vesicularity which we interpret as an increase in expansion of the  
676 clasts and a reduction in volume of the isolated vesicles. We interpret the fluidal and golden  
677 fragments, at the Main Vent, to be the faster and less degassed magma, which experienced  
678 only a very short residence time in the magma transport system (dyke+vent). According to  
679 previous work, these fragments should be derived from the central part of the fountains, but  
680 they do not show the strong post expansion signatures reported in the literature (Fig. 11). In  
681 fact they might represent the gas-rich magma with foam accumulation. In contrast, the spiny  
682 fragments from the Main Vent and the fluidal fragments from the Fractures show low  $N_v$  and  
683 low  $V_g/V_l$ . However, the presence of large numbers of isolated vesicles within the fluidal  
684 scoria from the Fractures agrees with their provenance from a fast hot ejection of relatively  
685 degassed magma (low  $N_v$ ). The higher percentage of microlites, the lack of isolated vesicles,  
686 the coalescence signature and the low  $N_v$  values of the spiny fragments (Fig. 4) are indicative  
687 of a extensively degassed and cooled magma. These clasts likely record the slowest ascent  
688 velocity and the longest residence time in the reservoir+dyke+vent system compared to the  
689 golden/fluidal counterpart (as suggested by similar clasts found also at Kilauea Iki, (Stovall et  
690 al., 2011).

691         Our findings are in full agreement with the recent review of Colombier et al. (2017b).  
692 According to these authors, connectivity values can be used as a useful tool to discriminate  
693 between the basaltic scoria from Hawaiian (fire fountaining) and Strombolian activity. The  
694 broad range in connectivity for pumice and scoria from fire fountaining is interpreted simply  
695 as being due to variations in the time available before quenching due to differences in location  
696 and residence time inside the fountain. The fluidal fragments from the Western Fractures are  
697 the richest in isolated vesicles because they are transported by very short lived hot lava jets. In



698 contrast, the higher connectivity observed in scoria from Strombolian activity is probably  
699 related to their higher average crystallinity, and more extensive degassing prior to the  
700 eruption, (Colombier et al., 2017b). The spiny surface of these Strombolian fragments is due  
701 to the fact that these weak explosions emit only a small solid mass fraction and the partially  
702 quenched dense clasts land quickly after a short cooling path through the surrounding  
703 atmosphere (e.g. Bombrun et al., 2015).

704 Among spiny fragments, the opaque ones are the densest, they lack a uniform glassy  
705 surface, and they are characterized by i) very high microlite content, ii) strong coalescence  
706 signature (Fig. 4), iii) heterogeneous glass chemistry, and iv) mingling with hotter magma at  
707 the edges (Fig. 8a). All these features reveal the composite nature of these clasts. We interpret  
708 the spiny opaque as spiny glass fragments recycled inside the eruptive vent during the  
709 explosions, being the densest portion of the magma prone to fall back in the vent/fracture  
710 (Fig. 2b).

711 Longitudinal variation in eruptive style along the fracture system produces a spatial  
712 variability in the proportions of the four typologies of clasts. The uppermost fractures are  
713 characterized solely by fluidal fragments; they lack both the spiny and the golden  
714 components. In addition, these fluidal clasts are the ones showing the smoothest surfaces  
715 (indicative of rapid quenching in a very hot environment), the lowest vesicularity, the highest  
716 content in isolated vesicles, but also by low vesicle numbers, comparable to the spiny  
717 fragments. These features are related to the emissions of only small amounts of partially  
718 degassed magma by short lived jets, which are clearly different from the sustained activity  
719 occurring at the Main Vent. The scoriae from the Fractures underwent rapid quenching in a  
720 very hot environment (jet of magma) that prevented any expansion or further vesiculation and  
721 preserved a very high number of isolated vesicles (Fig. 6d).

722 The four typologies of clasts were also found at the Main Vent, but with vertical  
723 variations in abundance from the base to the top, reflecting the variation in intensity and  
724 dynamics of the activity with time. It is interesting to note that the fluidal fragments at the  
725 Main Vent are less smooth (Fig. 4), more vesiculated, and have a lower content of isolated  
726 vesicles than the fluidal scoria from the uppermost Fractures (Fig. 6). Therefore fluidal  
727 fragments at the Main Vent could represent clasts that have been partly modified during their  
728 residence in the external part of the fountains, while the golden samples could come from the  
729 central part (Stovall et al., 2011 and 2012). However, the slight differences in crystallinity and  
730 glass chemistry between the fluidal and golden fragments support the idea that each of these  
731 fragments has an imprint from the pre-fragmentation setting. The spiny fragments are the



732 most degassed, densest and the most crystal rich magma that was emitted during low-energy  
733 activity by Strombolian explosion, where recycling phenomena were also very frequent (Fig.  
734 2f).

735

### 736 **5.3 Integration between the physical and textural characteristics of the products and** 737 **their geochemical signature: insight into the feeding system**

738 According to Peltier et al. (2016), the June 2014 eruption emitted magma from a shallow  
739 pressurized source located only 1.4-1.7 km below the volcano summit. Coppola et al. (2017)  
740 suggest that the 2014 event was fed by a single shallow and small volume magma pocket  
741 stored in the uppermost part of the PdF central plumbing system. All 2014 clasts show  
742 homogeneous and evolved bulk compositions, irrespective of their textural features. June  
743 2014 products are among the most evolved products erupted since at least 1998 and are  
744 moderately evolved with respect to those emitted in 2010, just before the 2010-2014  
745 quiescence. The different type of scoria and pumice show significant variations in glass  
746 composition (Fig. 8b) due to variable degrees of micro-crystallization. In theory, microlites  
747 and microphenocrysts can reflect late stage (during magma ascent and post-fragmentation)  
748 crystallization. In this case, their variable amount within, for instance, the glassy and opaque  
749 parts of the spiny scoria might reflect slower ascent velocity or longer residence time in the  
750 system (e.g. Hammer et al., 1999, Stovall et al., 2012; Gurioli et al., 2014) in agreement also  
751 with the vesicle signature. However, the four typologies of clasts differ in terms of mesocryst  
752 content (from rare to 5 vol% for the golden and fluidal and 14-23 vol% for the glassy spiny  
753 and spiny opaque, respectively). Equilibrium plagioclase-melt pairs record an almost constant  
754 and moderate dissolved water content, intermediate between that expected for melts sitting in  
755 the main shallow reservoir (located close to sea level) and the degassed matrix of lavas.  
756 Dissolved water contents are thus consistent with pre-eruptive magma water degassing at  
757 shallow level, as suggested by geophysical data, and suggest that the plagioclase mesocrysts  
758 and some of the microlites in the spiny scoria grew during magma storage. Melt composition  
759 records a potential pre-eruptive thermal gradient of  $\sim 30$  °C between the hotter (pumice and  
760 fluidal) and the cooler (spiny) magma.

761 Tait et al. (1989) suggest that magma evolution can lead to oversaturation of volatile  
762 species within a shallow reservoir and trigger a volcanic eruption. At PdF, the golden and the  
763 fluidal clasts might represent the portion of magma sitting in the shallow reservoir and  
764 accumulating bubbles of water rich fluids, released by the cooler, more crystallized and more



765 degassed “spiny” magma. The small volume of magma, its constant bulk composition and the  
766 very small inflation recorded prior to the eruption could be consistent with an internal source  
767 of pressure related to volatile exsolution. Larger inflation rates over a broader area are  
768 expected when reservoir pressurization is related to a new magma input from a deeper source.  
769 Textural heterogeneity of the 2014 products partly reflects a pre-eruptive thermal gradient  
770 recorded by the variability in crystal and bubble contents in the shallow reservoir feeding this  
771 eruption. Our results are consistent with processes of mechanical reservoirs/dyke  
772 stratification, as already observed experimentally by Menand and Phillips (2007). The golden  
773 and fluidal fragments are the bubble richer and hotter portion of the melt. The spiny fragments  
774 are the degassed and cooler portion of the reservoir, whose progressive tapping led to a  
775 decrease in explosive intensity (from fountaining to Strombolian activity). The spiny opaque  
776 clasts can be considered as being recycled material that fell back into the system.  
777 Accumulation of olivine crystals out of equilibrium with the host magma produces minor  
778 variations in phenocryst contents as observed within the same type of clasts sampled at  
779 different times/locations during the eruption, with the scoria from the Western Fracture and  
780 early erupted lava being the ones with the lowest amount of olivine (Table S4 and Fig. 7b).  
781 Again, this temporal variation supports a slight increase in heavy crystals within the most  
782 degassed magma emitted toward the end of activity, as observed as a general trend at PdF  
783 (Peltier et al., 2009).

784 Melt inclusion results allow us to confirm the involvement of a single and only slightly  
785 heterogeneous magma source in 2014, possibly related to cooling and fractional  
786 crystallisation of an older magma batch (November 2009). Interestingly, this latter short lived  
787 summit eruption was also characterized by the same large range of pyroclastic products in  
788 spite of the less evolved magmatic composition. The main difference with respect to 2014 is  
789 that the 2009 products contain a slightly larger amount of mm-sized olivine macrocrysts in the  
790 lava, scoria and pumice. This suggests that bubble accumulation and source pressurisation is  
791 mostly controlled by the shallow storage depth, which allows water exsolution (Di Muro et  
792 al., 2016), rather than by a trend of magma cooling and evolution (Tait et al., 1989).

793

794 **6. Conclusions** In this paper we show that a combination of textural and petro-chemical  
795 quantification of the eruptive products can be used to characterize the on-going activity at PdF  
796 and provide valuable information to understand both the causes and dynamics of these very  
797 short-lived and small-volume eruptions.





798           The June 2014 summit eruption occurred after a relatively long phase of quiescence  
799 and was preceded by only weak and short geophysical precursors. This multidisciplinary  
800 approach provides new constraints on the mechanisms triggering such short-lived, small  
801 eruptions. First, we found that this kind of eruption can be triggered solely by bubble  
802 accumulation and source pressurisation at a very shallow storage depth. We suggest that it is  
803 the shallow depth of the reservoir itself that allows exsolution, rather than magma cooling and  
804 evolution or recharge from a deep source. Second, these small, summit eruptions are usually  
805 related to small pockets of magma left behind following previous eruptions. Third, the  
806 thermal-mechanical stratification at the reservoir level between the bubble rich portion and  
807 the more degassed and cooler one modulates the style of the explosions. Therefore, in terms  
808 of ascent and degassing history of the magma the golden and fluidal fragments represent the  
809 bubble richer and hotter portion of the melt with faster ascent rate, while the spiny fragments  
810 are the degassed, cooler portion of the reservoir, whose progressive tapping lead to a decrease  
811 in explosive intensity (from fountaining to Strombolian activity). Finally, an accumulation of  
812 olivine crystals out of equilibrium with the host magma produces minor variations in  
813 phenocryst contents with a slight increase in heavy crystals within the most degassed magma  
814 emitted toward the end of activity, as observed as a general trend at PdF (Peltier et al., 2009).

815           To conclude, these results highlight the importance of petrological monitoring, which  
816 can provide complementary information regarding the ongoing volcanic activity to other  
817 geophysical and geochemical monitoring tools commonly used on volcanoes.

#### 818 **Acknowledgements**

819 OVPF team and T. Lecocq for monitoring and fieldwork. F. van Wyk de Vries provided an  
820 English revision for the proof. We thank the STRAP project funded by the Agence Nationale  
821 de la Recherche (ANR-14-CE03-0004-04). This research was financed by the French  
822 Government Laboratory of Excellence initiative no. ANR-10-LABX-0006, the Région  
823 Auvergne, and the European Regional Development Fund. This is Laboratory of Excellence  
824 Clervolc contribution number XXXX

825

#### 826 **References list**

827 Albarède, F., and V. Tamagnan (1988), Modelling the recent geochemical evolution of the  
828 Piton de la Fournaise volcano, Réunion island, 1931-1986, *J. Petrol.*, 29, 997-1030.



- 829 Albarède, F., B. Luais, G. Fitton, M.P. Semet, E. Kaminski, B.G.J Upton, P. Bachèlery, and  
830 J.L. Cheminée (1997), The geo-chemical regimes of Piton de la Fournaise Volcano Réunion.  
831 during the last 530,000 years, *J. Petrol.*, *38*, 171–201.
- 832 Andronico, D., M.D. Lo Castro, M. Sciotto, and L. Spina (2013a), The 2010 ash emissions at  
833 the summit craters of Mt Etna: relationship with seismo-acoustic signals, *J. Geophys. Res.*,  
834 *118*, 51–70, doi:10.1029/2012JB009895.
- 835 Andronico, D., J. Taddeucci, A. Cristaldi, L. Miraglia, P. Scarlato, and M. Gaeta (2013b), The  
836 15 March 2007 paroxysm of Stromboli: video-image analysis, and textural and compositional  
837 features of the erupted deposit, *Bull. Volcanol.*, *75*, 733, doi:10.1007/s00445-013-0733-2.
- 838 Andronico, D., S. Scollo, M.D. Lo Castro, A. Cristaldi, L. Lodato, and J. Taddeucci (2014),  
839 Eruption dynamics and tephra dispersal from the 24 November 2006 paroxysm at South-East  
840 Crater, Mt Etna, Italy, *J. Volcanol. Geotherm. Res.*, *274*, 78–91,  
841 doi:10.1016/j.jvolgeores.2014.01.009.
- 842 Bachèlery, P., J.F. Lénat, A. Di Muro, and L. Michon (2016), Active Volcanoes of the  
843 Southwest Indian Ocean: Piton de la Fournaise and Karthala. Active Volcanoes of the World.  
844 Springer-Verlag, Berlin and Heidelberg, 1-428, DOI 10.1007/978-3-642-31395-0\_12.
- 845 Boivin, P., and P. Bachèlery (2009), Petrology of 1977 to 1998 eruptions of Piton de la  
846 Fournaise, La Réunion Island, *J. Volcanol. Geotherm. Res.*, *184*, 109–125.
- 847 Boudoire, G., M. Liuzzo, A. Di Muro, V. Ferrazzini, L. Michon, F. Grassa, A. Derrien, N.  
848 Villeneuve, A. Bourdeu, C. Brunet, G. Giudice, and S. Gurrieri (2017), Investigating the  
849 deepest part of a volcano plumbing system: evidence for an active magma path below the  
850 western flank of Piton de la Fournaise (La Réunion Island), *J. Volcanol. Geotherm. Res.*, doi:  
851 10.1016/j.jvolgeores.2017.05.026.
- 852 Brenguier, F., P. Kowalski, T. Staudacher, V. Ferrazzini, F. Lauret, P. Boissier, A. Lemarchand,  
853 C. Pequegnat, O. Meric, C. Pardo, A. Peltier, S. Tait, N.M. Shapiro, M. Campillo, and A. Di  
854 Muro (2012), First Results from the UnderVolc High Resolution Seismic and GPS network  
855 deployed on Piton de la Fournaise Volcano, *Seismo. Res. Lett.* *83*(7),  
856 doi:10.1785/gssrl.83.1.97.



- 857 Brugier, Y.A. (2016), Magmatologie du Piton de la Fournaise (Ile de la Réunion): approche  
858 volcanologique, pétrologique et expérimentale. Sciences de la Terre. Université d'Orléans,  
859 NNT: 2016ORLE2007, pp. 251.
- 860 Bureau, H., F. Pineau, N. Métrich, P.M. Semet, and M. Javoy (1998a), A melt and fluid  
861 inclusion study of the gas phase at Piton de la Fournaise volcano (Reunion Island), *Chem.*  
862 *Geol.* *147*, 115–130.
- 863 Bureau, H., N. Métrich, F. Pineau, and M.P. Semet (1998b), Magma-conduit interaction at  
864 Piton de la Fournaise volcano (Réunion Island): a melt and fluid inclusion study, *J. Volcanol.*  
865 *Geotherm. Res.* *84*, 39–60.
- 866 Carey, R.J., M. Manga, W. Degruyter, D. Swanson, B. Houghton, T. Orr, and M. Patrick  
867 (2012), Externally triggered renewed bubble nucleation in basaltic magma: the 12 October  
868 2008 eruption at Halema'uma'u Overlook vent, Kīlauea, Hawai'i, USA, *J. Geophys. Res.*,  
869 *117*, B11202. doi:10.1029/2012JB009496.
- 870 Carey, R.J., M. Manga, W. Degruyter, H. Gonnermann, D. Swanson D, B. Houghton, T. Orr,  
871 and M. Patrick (2013), Convection in a volcanic conduit recorded by bubbles, *Geology*, *41*(4),  
872 395–398.
- 873 Cashman, K.V., and M.T. Mangan (1994) Physical aspects of magmatic degassing II:  
874 constraints on vesiculation processes from textural studies of eruptive products, In: Carroll  
875 MR, Holloway JR (eds) Volatiles in magmas, Reviews in mineralogy. *Miner. Soc. Am.*,  
876 Fredricksberg, pp 447–478.
- 877 Clocchiatti, R., A. Havette, and P. Nativel (1979), Relations pétrogénétiques entre les basaltes  
878 transitionnels et les océanites du Piton de la Fournaise (Ile de la Réunion, océan Indien) à  
879 partir e la composition chimique des inclusions vitreuses des olivines et des spinelles, *Bull.*  
880 *Minér.*, *102*, 511–525.
- 881 Colombier, M., L. Gurioli, T.H. Druitt, T. Shea, P. Boivin, D. Miallier, and N. Cluzel (2017a),  
882 Textural evolution of magma during the 9.4-ka trachytic explosive eruption at Kilian Volcano,  
883 Chaîne des Puys, France, *Bull. Volcanol.*, *79*(2), 1-24. doi:10.1007/s00445-017-1099-7.
- 884 Colombier, M., F.B. Wadsworth, L. Gurioli, B. Scheu, U. Kueppers, A. Di Muro, and D.B.  
885 Dingwel (2017b), The evolution of pore connectivity in volcanic rocks, *Earth Planet. Sci.*  
886 *Lett.*, *462*, 99-109. DOI: 10.1016/j.epsl.2017.01.011.



- 887 Colò, L., M. Ripepe, D.R. Baker, and M. Polacci (2010), Magma vesiculation and infrasonic  
888 activity at Stromboli open conduit volcano, *Earth Planet. Sc. Lett.* 292(3–4):274–280.
- 889 Coppola, D., N. Villeneuve, A. Di Muro, V. Ferrazzini, A. Peltier, M. Favalli, P. Bachèlery, L.  
890 Gurioli, A. Harris, S. Moune, I. Vlastélic, B. Galle, S. Arellano, and A. Aiuppa (2017), A  
891 Shallow system rejuvenation and magma discharge trends at Piton de la Fournaise volcano  
892 (La Réunion Island), *Earth Planet. Sci. Lett.* 463, 13-24.
- 893 Corsaro, R., and L. Miraglia (2014), The transition from summit to flank activity at Mt. Etna,  
894 Sicily (Italy): Inferences from the petrology of products erupted in 2007–2009, *J. Volcanol.*  
895 *Geother. Res.*, 275, 51– 60.
- 896 Di Muro, A., Métrich, N., Vergani, D., Rosi, M., Armienti, P., Fougeroux, T., Deloule, E.,  
897 Arienzo, I., Civetta, L. (2014), The shallow plumbing system of Piton de la Fournaise Volcano  
898 (La Réunion Island, Indian Ocean) revealed by the major 2007 caldera forming eruption, *J.*  
899 *Petrol.*, 55, 1287-1315.
- 900 Di Muro, A., T. Staudacher, V. Ferrazzini, N. Métrich, P. Besson, C. Garofalo, and B.  
901 Villemant (2015), Shallow magma storage at Piton de la Fournaise volcano after 2007 summit  
902 caldera collapse tracked in Pele’s hairs, chap 9 of Carey, R. J., V. Cayol, M. P. Poland, and D.  
903 Weis (eds.), Hawaiian Volcanoes: From Source to Surface, *American Geophysical Union*  
904 *Monograph 208*, pp 189–212, doi:10.1002/9781118872079.ch9.
- 905 Di Muro, A., N. Métrich, P. Allard, A. Aiuppa, M. Burton, B. Galle, and T. Staudacher (2016),  
906 Magma degassing at Piton de la Fournaise volcano, Active Volcanoes of the World, series,  
907 Springer, Bachelery, P., Lenat, J.F, Di Muro, A., Michon L., Editors. Pg. 203-222.
- 908 Eychenne, J., B.F. Houghton, D.A. Swanson, R.J. Carey, and L. Swavely (2015), Dynamics of  
909 an open basaltic magma system: the 2008 activity of the Halema‘uma‘u Overlook vent,  
910 Kīlauea Caldera. *Earth Planet. Sci. Lett.*, 409, 49–60.
- 911 Famin, V., B. Welsch, S. Okumura, P. Bachèlery, and S. Nakashima (2009), Three  
912 differentiation stages of a single magma at Piton de la Fournaise (Réunion hotspot). *Geoch.*  
913 *Geoph. Geos.* 10, Q01007. doi:10. 1029/2008GC002015.
- 914 Fisk, M.R., B.G.J Upton, C.E. Ford, and W.M. White (1988), Geochemical and experimental  
915 study of the genesis of magmas of Reunion island, Indian Ocean, *J. Geophys. Res.*, 93, 4933-  
916 4950.



- 917 Formenti, Y, and T.H. Druitt (2003), Vesicle connectivity in pyroclasts and implications for  
918 the fluidisation of fountain-collapse pyroclastic flows, Montserrat (West Indies), *Earth Planet.*  
919 *Sci. Lett.*, *214*, 561–574.
- 920 Gardner, J.E., R.M.E. Thomas, C. Jaupart, and S. Tait (1996), Fragmentation of magma  
921 during Plinian volcanic eruptions, *Bull. Volcanol.*, *58*, 144–162.
- 922 Giachetti, T., T.H. Druitt, A. Burgisser, L. Arbaret, and C. Galven (2010), Bubble nucleation  
923 and growth during the 1997 Vulcanian explosions of Soufrière Hills Volcano, Montserrat, *J.*  
924 *Volcanol. Geotherm. Res.*, *193*(3–4):215–231. doi:10.1016/j.jvolgeores.2010.04.001.
- 925 Gonnermann, H.M., and M. Manga (2013) Dynamics of magma ascent in the volcanic  
926 conduit. In: Fagents, S.A., Gregg, T.K.P., Lopes, R.M.C. (Eds.), *Modeling Volcanic Processes:*  
927 *The Physics and Mathematics of Volcanism*. Cambridge University Press, Cambridge.
- 928 Gurioli, L., A.J.L. Harris, L. Colo, J. Bernard, M. Favalli, M. Ripepe, and D. Andronico  
929 (2013), Classification, landing distribution and associated flight parameters for a bomb field  
930 emplaced during a single major explosion at Stromboli, Italy, *Geology*, *41*, 559-562, DOI  
931 10.1130/G33967.1.
- 932 Gurioli, L., L. Colo', A.J. Bolasina, A.J.L. Harris, A. Whittington, and M. Ripepe (2014),  
933 Dynamics of strombolian explosions: inferences from inferences from field and laboratory  
934 studies of erupted bombs from Stromboli volcano, *J. Geophys. Res.*, *119*(1),  
935 DOI:10.1002/2013JB010355.
- 936 Gurioli, L., D. Andronico, P. Bachelery, H. Balcone-Boissard, J. Battaglia, G. Boudon, A.  
937 Burgisser, S.B. M.R. Burton, K. Cashman, S. Cichy, R. Cioni, A. Di Muro, L. Dominguez, C.  
938 D'Oriano, T. Druitt, A.J.L Harris, M. Hort, K. Kelfoun, J.C. Komorowski, U. Kueppers, J.L.  
939 Le Pennec, T. Menand, R. Paris, L. Pioli, M. Pistolesi, M. Polacci, M. Pompilio, M. Ripepe,  
940 O. Roche, E. Rose-Koga, A. Rust, L. Scharff, F. Schiavi, R. Sulpizio, J. Taddeucci, and T.  
941 Thordarson (2015), MeMoVolc consensual document: a review of cross-disciplinary  
942 approaches to characterizing small explosive magmatic eruptions, *Bull. Volcanol.*, *77*, 49.  
943 DOI: 10.1007/s00445-015-0935-x.
- 944 Helz, R.T., and C.R. Thorber (1987), Geothermometry of Kilauea Iki lava lake, Hawaii, *Bull.*  
945 *Volcanol.*, *49*, 651–668.



- 946 Hibert, C, A. Mangeney, M. Polacci, A. Di Muro, S. Vergnolle, V. Ferrazzini, B. Taisne, M.  
947 Burton, T. Dewez, G. Grandjean, A. Dupont, T. Staudacher, F. Brenguier, N.M. Shapiro, P.  
948 Kowalski, P. Boissier, P. Catherine, and F. Lauret (2015), Multidisciplinary monitoring of the  
949 January 2010 eruption of Piton de la Fournaise volcano, La Réunion island, *J. Geophys. Res.*,  
950 *120*(5), 3026-3047
- 951 Houghton, B.F., and C.J.N. Wilson (1989), A vesicularity index for pyroclastic deposits, *Bull.*  
952 *Volcanol.*, *51*, 451–462. doi:10.1007/BF01078811
- 953 Houghton, B.F., D.A. Swanson, R.J. Carey, J Rausch., and A.J Sutton (2011), Pigeonholing  
954 pyroclasts, insights from the 19 March 2008 explosive eruption of Kīlauea volcano,  
955 *Geology*,*39*, 263–266, doi:10.1130/G31509.1.
- 956 Houghton, B.F., D.A. Swanson, J. Rausch, R.J. Carey, Fagents S.A., and T.R. Orr (2013),  
957 Pushing the volcanic explosivity index to its limit and beyond: constraints from exceptionally  
958 weak explosive eruptions at Kīlauea in 2008, *Geology*, *41*(6):627–630
- 959 Houghton, B.F., J. Taddeucci, D. Andronico, H.M. Gonnermann, M. Pistolesi, M.R. Patrick,  
960 T.R. Orr, D.A. Swanson, M.Edmonds, D. Gaudin, R.J. Carey and P. Scarlato (2016), Stronger  
961 or longer: Discriminating between Hawaiian and Strombolian eruption styles, *Geology* doi:  
962 10.1130/G37423.1
- 963 Kahl, M., S.Chakraborty, M. Pompilio, and F. Costa (2015), Constraints on the nature and  
964 evolution of the magma plumbing system of Mt. Etna Volcano (1991–2008) from a combined  
965 thermodynamic and kinetic modelling of the compositional record of minerals, *J.Petrol.*, *56*,  
966 2025–2068, doi:10.1093/petrology/egv063.
- 967 Kawabata, E., S.J. Cronin, M.S. Bebbington, M.R.H. Moufti, N. El-Masry, and T. Wang  
968 (2015), Identifying multiple eruption phases from a compound tephra blanket: an example of  
969 the AD1256 Al-Madinah eruption, Saudi Arabia, *Bull. Volcanol.*, *77*, 6 DOI 10.1007/s00445-  
970 014-0890-y.
- 971 Lange, A.L., H.M. Frey, and J. Hector (2009), A thermodynamic model for the plagioclase-  
972 liquid hygrometer/thermometer, *Am. Mineral.*, *94*, 494–506.
- 973 Lautze, N., J. Taddeucci, D. Andronico, C. Cannata, L. Tornetta, P. Scarlato, B. Houghton, and  
974 D. Lo Castro (2012), SEM-based methods for the analysis of basaltic ash from weak



975 explosive activity at Etna in 2006 and the 2007 eruptive crisis at Stromboli, *Phys. Chem.*  
976 *Earth* 45,46, 113–127, doi:10.1016/j.pce.2011.02.001.

977 Leduc, L., L. Gurioli, A.J.L. Harris, L. Colo', and E. Rose-Koga (2015), Types and  
978 mechanisms of strombolian explosions: characterization of a gas-dominated explosion at  
979 Stromboli, *Bull. Volcanol.*, 77, 8, DOI: 10.1007/s00445-014-0888-5

980 Leibbrandt, S, and J.L. Le Penneec (2015), Towards fast and routine analyses of volcanic ash  
981 morphometry for eruption surveillance applications, *J. Volcanol. Geotherm. Res.*, 297, 11–27.

982 Lénat, E.F., P.B. Bachelery, and O. Merle (2012), Anatomy of Piton de la Fournaise volcano  
983 (La Réunion, Indian Ocean), *Bull. Volcanol.* 74, 1945–1961.

984 Lengliné, O, Z. Duputel, and V. Ferrazzini (2016), Uncovering the hidden signature of a  
985 magmatic recharge at Piton de la Fournaise volcano using small earthquakes, *Geophys. Res.*  
986 *Let.*, 43, doi: 10.1002/2016GL068383

987 Mangan, M.T., and K.V. Cashman (1996), The structure of basaltic scoria and reticulite and  
988 inferences for vesiculation, foam formation, and fragmentation in lava fountains. *J. Volcanol.*  
989 *Geotherm. Res.*, 73, 1–18.

990 Menand, T., and J.C. Phillips (2007), Gas segregation in dykes and sills. *J. Volcanol. Geother.*  
991 *Res.*, 159(4), 393–408. <https://doi.org/10.1016/j.jvolgeores.2006.08.003>.

992 Michon, L., A. Di Muro, N. Villeneuve, C. Saint-Marc, P. Fadda, and F. Manta (2013),  
993 Explosive activity of the summit cone of Piton de la Fournaise volcano (La Réunion Island): a  
994 historical and geological review, *J. Volcanol. Geotherm. Res.* 263, 117-133.

995 Moune, S., O. Sigmarsson, P. Schiano, T. Thordarson, and J.K. Keiding (2012), Melt  
996 inclusion constraints on the magma source of Eyjafjallajökull 2010 flank eruption, *J.*  
997 *Geophys. Res.*, 117, B00C07, doi:10.1029/2011jb008718.

998 Morandi, A., C. Principe, A. Di Muro, G. Leroi, L. Michon, and P. Bachèlery (2016), Pre-  
999 historic explosive activity at Piton de La Fournaise volcano. In: Bachèlery P, Lénat JF, Di  
1000 Muro A, Michon L (eds) Active Volcanoes of the Southwest Indian Ocean: Piton de la  
1001 Fournaise and Karthala. Active Volcanoes of the World. Springer-Verlag, Berlin and  
1002 Heidelberg, pp 107–138



- 1003 Óladóttir, B., O. Sigmarsson, G. Larsen, and J.-L. Devidal (2011), Provenance of basaltic  
1004 tephra from Vatnajökull subglacial volcanoes, Iceland, as determined by major- and trace-  
1005 element analyses, *Holocene*, 21, 1037–1048, doi:10.1177/0959683611400456.
- 1006 Ort, M.H., A. Di Muro, L. Michon, and P. Bachèlery (2016), Explosive eruptions from the  
1007 interaction of magmatic and hydrothermal systems during flank extension: the Bellecombe  
1008 Tephra of Piton de La Fournaise (La Réunion Island), *Bull. Volcanol.* 78, 5,  
1009 doi:10.1007/s00445-015-0998-8.
- 1010 Papale P., R. Moretti, and D. Barbato (2006), The compositional dependence of the saturation  
1011 surface of H<sub>2</sub>O + CO<sub>2</sub> fluids in silicate melts, *Chemical Geology*, 229, 1/3, 78-95,  
1012 doi:10.1016/j.chemgeo.2006.01.013.
- 1013 Parcheta, C.E., B.F. Houghton, and D.A. Swanson (2013), Contrasting patterns of vesiculation  
1014 in low, intermediate, and high Hawaiian fountains: a case study of the 1969 Mauna Ulu  
1015 eruption, *J. Volcanol. Geotherm. Res.*, 255, 79–89
- 1016 Peltier, A., F. Beauducel, N. Villeneuve, V. Ferrazzini, A. Di Muro, A. Aiuppa, A. Derrien, K.  
1017 Jourde, and B. Taisne (2016), Deep fluid transfer evidenced by surface deformation during the  
1018 2014–2015 unrest at Piton de la Fournaise volcano, *J. Volcanol. Geotherm. Res.*, 321, 140–  
1019 148. <http://dx.doi.org/10.1016/j.jvolgeores.2016.04.031>.
- 1020 Peltier, A., P. Bachèlery, and T. Staudacher (2009), Magma transport and storage at Piton de la  
1021 Fournaise (La Réunion) between 1972 and 2007: A review of geophysical and geochemical  
1022 data. *J. Volcanol. Geotherm. Res.*, 184, 93-108.
- 1023 Polacci, M., R. Corsaro, and D. Andronico (2006a), Coupled textural and compositional  
1024 characterization of basaltic scoria: insights into the transition from Strombolian to fire  
1025 fountain activity at Mount Etna, Italy, *Geology*, 34(3), 201–204. doi:10.1130/G223181.1.
- 1026 Polacci, M., C. Bouvet de Maisonneuve, D. Giordano, M. Piochi, L. Mancini L., W.  
1027 Degruyter, and O. Bachmann (2014), Permeability measurements of Campi Flegrei  
1028 pyroclastic products: an example from the Campanian Ignimbrite and Monte Nuovo  
1029 eruptions. *J. Volcanol. Geotherm. Res.* 272, 16–22.
- 1030 Putirka, K.D. (2008), Thermometers and barometers for volcanic systems, *Rev. Mineral.*  
1031 *Geochem.* 69, 61-120.





- 1032 Roeder, P., E. Goffin, and C. Thornber (2006), Cotectic proportions of olivine and spinel in  
1033 olivine-tholeiitic basalt and evaluation of pre-eruptive processes, *J. Petrol.*, *47*, 883-900.
- 1034 Roullet, G., A. Peltier, T. Staudacher, V. Ferrazzini, B. Taisne, A. Di Muro, and The OVPF Team  
1035 (2012), A comprehensive classification of the Piton de la Fournaise eruptions (La Réunion  
1036 Island) spanning the 1986–2010 period. Search for eruption precursors from the broad-band  
1037 GEOSCOPE RER station analysis and interpretation in terms of volcanic processes, *J.*  
1038 *Volcanol. Geotherm. Res.*, *241*, 78–104.
- 1039 Rust, A.C., and K.V. Cashman (2011), Permeability controls on expansion and size  
1040 distributions of pyroclasts, *J. Geophys. Res.*, *116*, B11202.
- 1041 Salaün, A., Villemant, B., Semet, M.P., and T. Staudacher (2010), Cannibalism of olivine-rich  
1042 cumulate xenoliths during the 1998 eruption of Piton de la Fournaise (La Réunion hotspot):  
1043 Implications for the generation of magma diversity. *J. Volcanol. Geother. Res.*, *198*, 187-204.
- 1044 Schiano, P., K. David, I. Vlastélic, A. Gannoun, M. Klein, F. Nauret, and Bonnard P. (2012),  
1045 Osmium isotope systematics of historical lavas from Piton de la Fournaise (Réunion Island,  
1046 Indian Ocean), *Contrib. Mineral. Petrol.*, <http://dx.doi.org/10.1007/s00410-012-0774-0>.
- 1047 Shea, T., B.F. Houghton, L. Gurioli, K.V. Cashman, J.E. Hammer, and B. Hobden (2010),  
1048 Textural studies of vesicles in volcanic rocks: an integrated methodology, *J. Volcanol.*  
1049 *Geotherm. Res.*, *190*, 271–289.
- 1050 Shea, T., L. Gurioli, and B.F. Houghton (2012), Transitions between fall phases and  
1051 pyroclastic density currents during the AD 79 eruption at Vesuvius: building a transient  
1052 conduit model from the textural and volatile record, *Bull. Volcanol.*, *74*, 2363–2381,  
1053 doi:10.1007/s00445-012-0668-z.
- 1054 Sparks, R.S.J. (1978), The dynamics of bubble formation and growth in magmas: a review  
1055 and analysis, *J. Volcanol. Geotherm. Res.*, *3*, 1–37.
- 1056 Sparks, R.S.J. (2003). Forecasting volcanic eruptions, *Earth Planet. Sci. Lett.*, *210*, 1–15.
- 1057 Staudacher, T., and A. Peltier (2015), Ground deformation at Piton de la Fournaise (La  
1058 Réunion Island), a review from 20 years of GNSS monitoring, In: Bachèlery P, Lénat, JF, Di  
1059 Muro A, Michon L (ed) Active volcanoes of the Southwest Indian Ocean: Piton de la



- 1060 Fournaise and Karthala. Active volcanoes of the world. Springer, Berlin, 139-170.  
1061 doi:10.1007/978-3-642-31395-0\_9
- 1062 Staudacher, T., V. Ferrazzini, A. Peltier, P. Kowalski, P. Boissier, P. Catherine, F. Lauret, and  
1063 F. Massin (2009), The April 2007 eruption and the Dolomieu crater collapse, two major  
1064 events at Piton de la Fournaise (La Reunion Island, Indian Ocean). *J. Volcanol. Geother. Res.*  
1065 *184*, 126-137, doi:10.1016/j.jvolgeores.2008.11.005.
- 1066 Stovall, W.K., B.F. Houghton, H.M. Gonnermann, S.A. Fagents, and D.A. Swanson (2011),  
1067 Eruption dynamics of Hawaiian-style fountains: the case study of episode 1 of the Kīlauea Iki  
1068 1959 eruption, *Bull. Volcanol.* *73*, 511–529. doi:10.1007/s00445-010-0426-z.
- 1069 Stovall, W.K., B.F. Houghton, J.E. Hammer, S.A. Fagents, and D.A. Swanson (2012),  
1070 Vesiculation of high fountaining Hawaiian eruptions: episodes 15 and 16 of 1959 Kīlauea Iki,  
1071 *Bull. Volcanol.*, *74*, 441–455, doi:10.1007/s00445-011-0531-7.
- 1072 Swanson, D.A., K. Wooten, and T. Orr (2009), Buckets of ash track tephra flux from  
1073 Halema‘ūma‘u crater, Hawai‘i. *Eos Trans. AGU*, *90*, 427–428. doi:10.1029/2009EO460003.
- 1074 Taddeucci, J., M. Pompilio, and P. Scarlato (2002), Monitoring the explosive activity of the  
1075 July–August 2001 eruption of Mt. Etna (Italy) by ash characterization, *Geophys. Res. Lett.*,  
1076 *29*(8), 1029–1032. doi:10.1029/2001GL014372.
- 1077 Tait, S., C. Jaupart, and S. Vergnolle (1989), Pressure, gas content and eruption periodicity of  
1078 a shallow, crystallising magma chamber, *Earth Planet. Sci. Lett.*, *92*, 107-123.
- 1079 Thornber, C.R., K. Hon, C. Heliker, and D.A. Sherrod (2003), A Compilation of Whole-Rock  
1080 and Glass Major-Element geochemistry of Kīlauea Volcano, Hawai‘i, near-vent eruptive  
1081 products: January 1983 through September 2001: *U.S.G.S. Open File Report*, 03-477.
- 1082 Thordarson, T, S Self, N Óskarsson, and T Hulsebosch (1996), Sulfur, chlorine and fluorine  
1083 degassing and atmospheric loading by the 1783–1784 AD Laki (Skaftár Fires) eruption in  
1084 Iceland, *Bull. Volcanol.* *58*, 205–225.
- 1085 Villemant, B., A. Salaün, and T. Staudacher (2009), Evidence for a homogeneous primary  
1086 magma at Piton de la Fournaise (La Réunion): A geochemical study of matrix glass, melt  
1087 inclusions and Pélé’s hairs of the 1998–2008 eruptive activity, *J. Volcanol. Geotherm. Res.*,  
1088 *184*, 79–92.

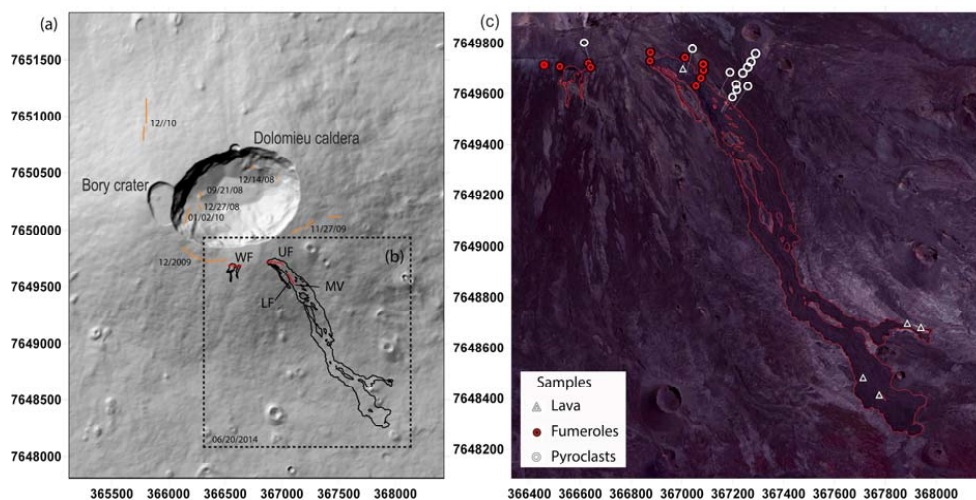


- 1089 Vlastélic, I., and A.J. Pietruszka (2016), A review of the recent geochemical evolution of  
1090 Piton de la Fournaise Volcano (1927–2010). In: Bachèlery, P., Lénat, J.F., Di Muro, A.,  
1091 Michon, L. (Eds.), Active Volcanoes of the Southwest Indian Ocean. In: Active Volcanoes of  
1092 the World, pp.185–201.
- 1093 Vlastélic, I., T. Staudacher, and M. Semet (2005), Rapid change of lava composition from  
1094 1998 to 2002 at Piton de la Fournaise (Réunion) inferred from Pb isotopes and trace elements:  
1095 evidence for variable crustal contamination, *J. Petrol.* *46*, 79-107.
- 1096 Vlastélic, I., A. Peltier, and T. Staudacher (2007), Short-term (1998–2006) fluctuations of Pb  
1097 isotopes at Piton de la Fournaise volcano (Réunion Island): origins and constraints on the size  
1098 and shape of the magma reservoir, *Chem. Geology*, *244*, 202-220.
- 1099 Vlastélic, I., C. Deniel, C. Bosq, P. Telouk, P. Boivin, P. Bachèlery, V. Famin, and T.  
1100 Staudacher (2009), Pb isotope geochemistry of Piton de la Fournaise historical lavas, *J.*  
1101 *Volcanol. Geother. Res.*, *184*, 63-78.
- 1102 Vlastélic, I., G. Menard, M. Gannoun, J.-L. Piro, T. Staudacher, and V. Famin (2013), Magma  
1103 degassing during the April 2007 collapse of Piton de la Fournaise: the record of semi-volatile  
1104 trace elements (Li, B, Cu, In, Sn, Cd, Re, Tl, Bi), *J. Volcanol. Geother. Res.*, *254*, 94-107.
- 1105 Vlastélic, I., A. Gannoun, A. Di Muro, L. Gurioli, P. Bachèlery, and J.M. Henot (2016), Origin  
1106 and fate of sulfide liquids in hotspot volcanism (La Réunion): Pb isotope constraints from  
1107 residual Fe–Cu oxides, *Geochim. Cosmochim. Acta*, *194*, 179-192.
- 1108 Welsch, B., F. Faure, P. Bachèlery, and V. Famin (2009), Microcrysts record transient  
1109 convection at Piton de la Fournaise volcano (La Réunion Hotspot), *J. Petrol.*, *50*, 2287-2305.
- 1110 Welsch, B., V. Famin, A. Baronnet, and P. Bachèlery (2013), Dendritic crystallization: a single  
1111 process for all textures of olivine in basalts? *J. Petrol.*, *54*, 539-574.
- 1112 White, J.D.L., and B.F. Houghton (2006), Primary volcanoclastic rocks, *Geology*, *34*, 677–  
1113 680, doi:10.1130/G22346.1.

1114 **Figure captions**

1115

1116



1117

1118 **Figure 1** a) Digital elevation model of the summit crater area at Piton de La Fournaise, la  
1119 Réunion, France; orange = fractures generated by pre-2014 eruptions; b) red = fractures active  
1120 during the 2014 eruption: WF (western fracture), UF (upper fracture), LF (lower fracture),  
1121 MV (Main Vent). Black= outline of the 2014 lava field; c) location of sample collection points

1122

1123

1124

1125

1126

1127

1128

1129

1130

1131

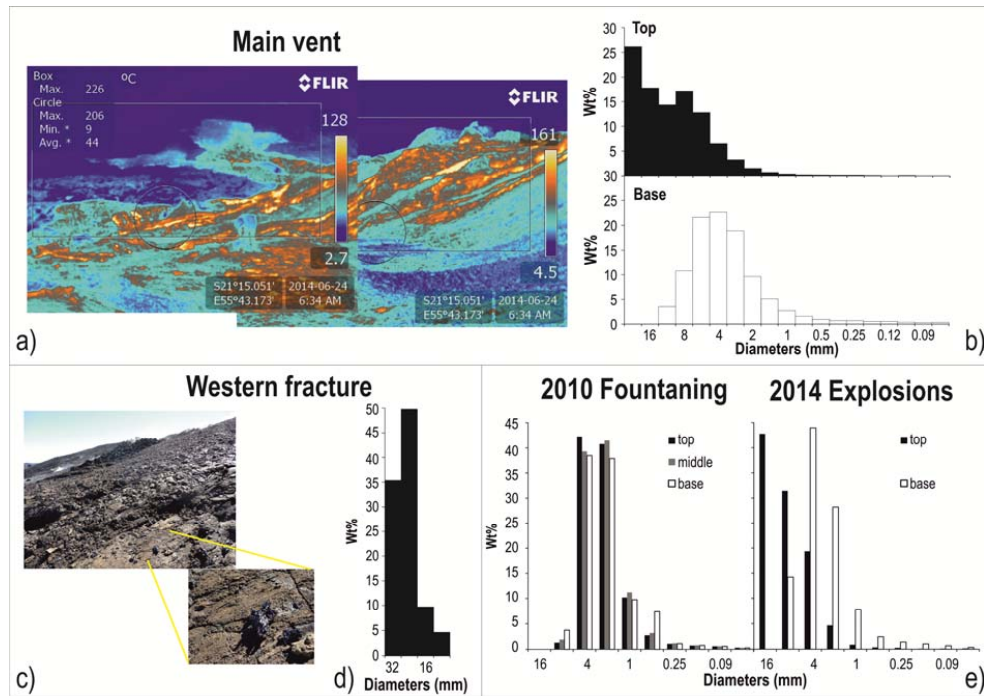
1132

1133



1134

1135 **Figure 2** Photo collection from the web site. From a to f: evolution of activity from early  
1136 morning to evening, June 21. All the photos are from the Main Vent (see Fig. 1). The images  
1137 in a, b and the inset in b are from Laurent Perrier; c) [http://www.rtl.fr/actu/sciences-](http://www.rtl.fr/actu/sciences-environnement/la-reunion-eruption-du-piton-de-la-fournaise-apres-4-ans-de-sommeil-7772778861)  
1138 [environnement/la-reunion-eruption-du-piton-de-la-fournaise-apres-4-ans-de-sommeil-](http://www.rtl.fr/actu/sciences-environnement/la-reunion-eruption-du-piton-de-la-fournaise-apres-4-ans-de-sommeil-7772778861)  
1139 [7772778861](http://www.rtl.fr/actu/sciences-environnement/la-reunion-eruption-du-piton-de-la-fournaise-apres-4-ans-de-sommeil-7772778861); d) [http://www.ipreunion.com/volcan/reportage/2014/06/21/eruption-du-piton-](http://www.ipreunion.com/volcan/reportage/2014/06/21/eruption-du-piton-de-la-fournaise-actualise-a-17h-la-lave-coule-sur-1-5-kilometre.26023.html)  
1140 [de-la-fournaise-actualise-a-17h-la-lave-coule-sur-1-5-kilometre.26023.html](http://www.ipreunion.com/volcan/reportage/2014/06/21/eruption-du-piton-de-la-fournaise-actualise-a-17h-la-lave-coule-sur-1-5-kilometre.26023.html); e)  
1141 [http://www.zinfos974.com/L-eruption-du-Piton-de-la-Fournaise-Le-point-de-](http://www.zinfos974.com/L-eruption-du-Piton-de-la-Fournaise-Le-point-de-17h_a72981.html)  
1142 [17h\\_a72981.html](http://www.zinfos974.com/L-eruption-du-Piton-de-la-Fournaise-Le-point-de-17h_a72981.html); f) <http://nancyroc.com/eruption-a-la-reunion>



1143

1144 **Figure 3** a) Thermal photo of the scoria fall out area in proximity to the Main Vent (see Fig. 1  
1145 for the location); b) grain size histograms for the base and top deposit of the Main Vent; c)  
1146 scattered scoria from the Western Fracture (see Fig. 1 for the location); d) grain size histogram  
1147 of the scoria deposit at the Western Fracture; e) comparison between the grain size histograms  
1148 for the 2010 Hawaiian fountaining and the 2014 Main vent activity

1149

1150

1151

1152




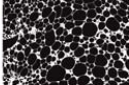
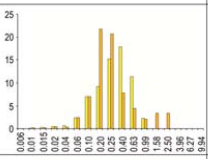



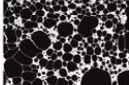
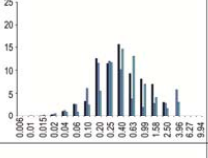


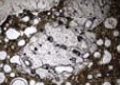

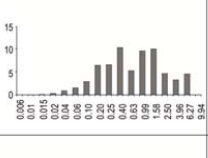
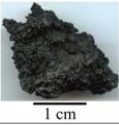
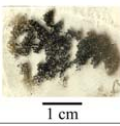


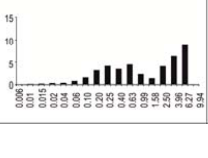
1153

1154

1155

1156



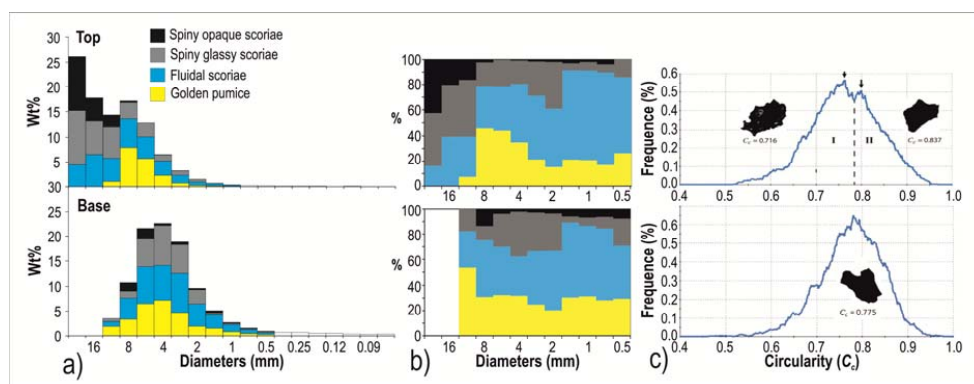
Type	Clast	Thin section	Microscope	SEM (25X)	VSD (%; mm)	%cry	N <sub>v</sub>
Golden Pumice (a)			 0.02 mm			Meso = (rare) Micro = (14-15)	$2 \times 10^7$ $9 \times 10^5$
Fluidal Scoria (b)			 0.02 mm			Meso = (0-5) Micro = (14-29)	$2 \times 10^7$ $5 \times 10^6$ $3 \times 10^5$
Spiny glassy scoria (c)			 0.02 mm			Meso = (14) Micro = (25)	$6 \times 10^5$
Spiny opaque scoria (d)			 0.02 mm			Meso = (23) Micro = (31)	$4 \times 10^5$

1157

1158 **Figure 4** Textural features of the 2014 pyroclasts. Clast = photo of the different types of  
 1159 juvenile pyroclasts. Thin section = thin section imaged with a desktop scanner. Microscope =  
 1160 photo taken with an optical microscope using natural light; SEM (25X) = photo captured  
 1161 using a scanning electron microscopy (SEM), in BSE mode at 25x magnification: black are  
 1162 vesicles, white is glass, grey are crystals. VSD = vesicle volume distribution histograms,  
 1163 where the diameter, in mm, is plotted versus the volume percentage. %Cry = is the total  
 1164 percentage of crystals corrected for the vesicularity. N<sub>v</sub> = number density

1165

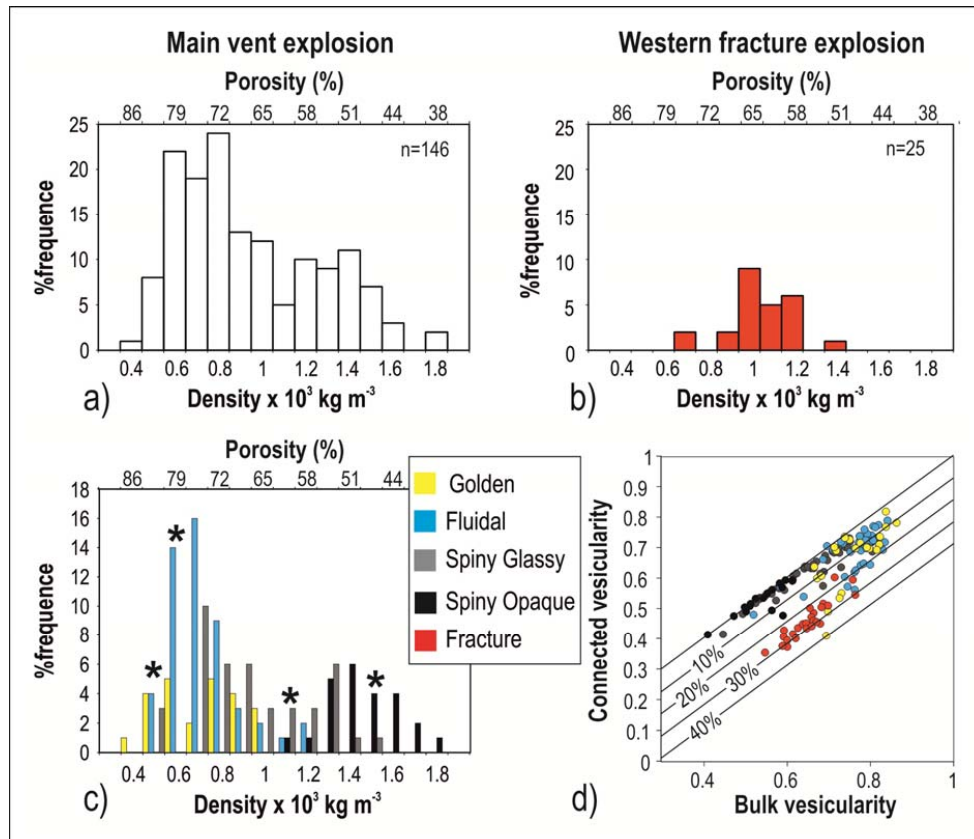
1166



1167

1168 **Figure 5** Proportion of each type of clast measured from the Main Cone for the 2014  
1169 eruption: (a) componentry within the different grain size classes from the base to the top of a  
1170 10 cm thick scoria deposit; b) normalized componentry composition from the base to the top  
1171 of the deposits; c) Morphologi G3 results for the coarse ash fragments (350 micron), where  
1172 the population is formed exclusively of smooth fragments that correspond to fluidal and  
1173 golden pumice.





1174

1175 **Figure 6** Density and connectivity data of the 2014 pyroclast fragments: a) density  
 1176 distribution histogram for all the pyroclast fragments measured for the 2014 activity from the  
 1177 Main Vent; b) for the Western fracture; and c) for different typologies of clasts from the Main  
 1178 Vent; d) graph of connected vesicularity versus total vesicularity. The diagonal line represents  
 1179 equality between the connectivity and vesicularity, beneath this line the samples have isolated  
 1180 vesicles

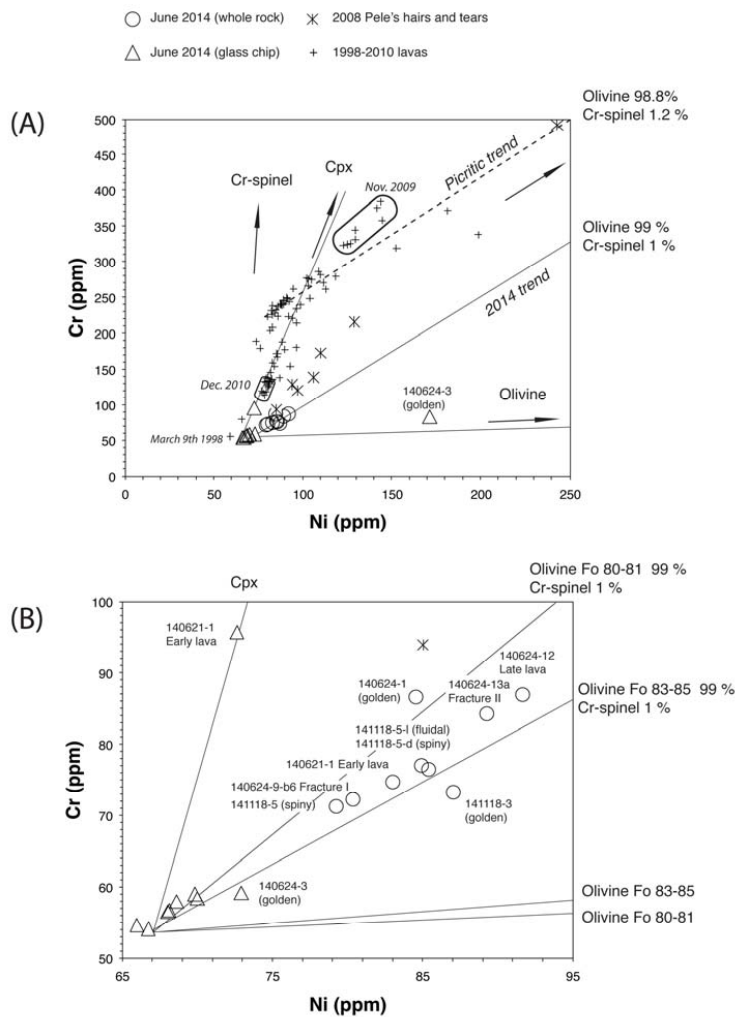
1181

1182

1183

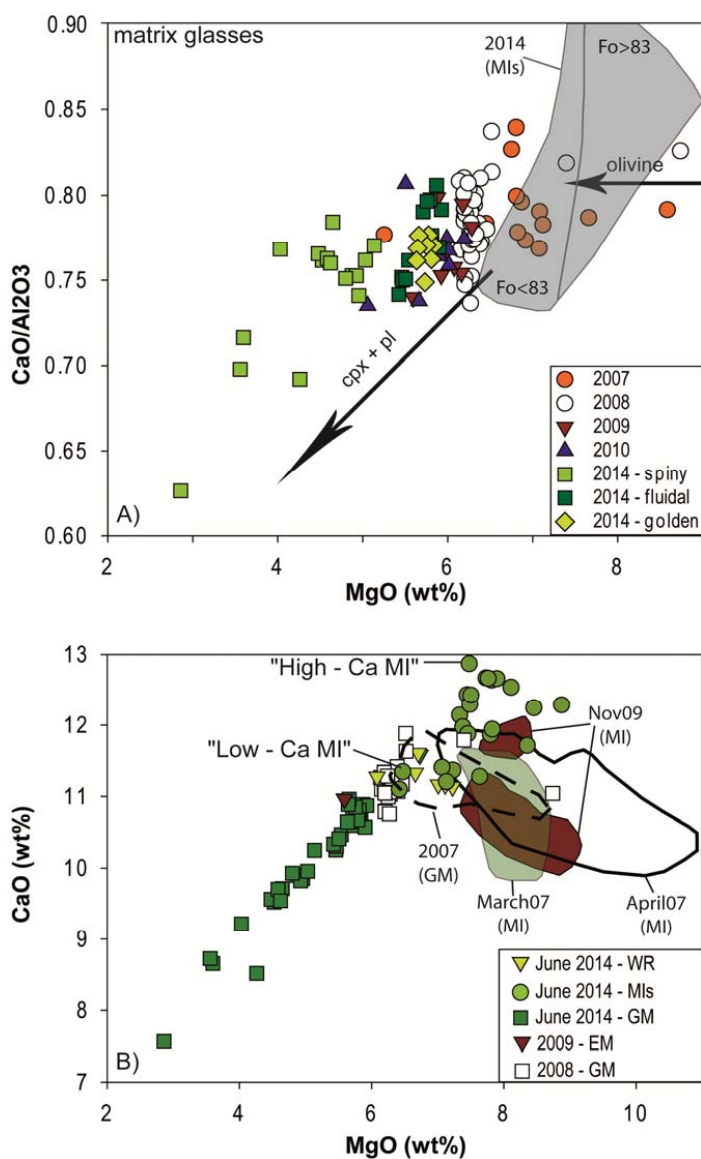
1184

1185



1186

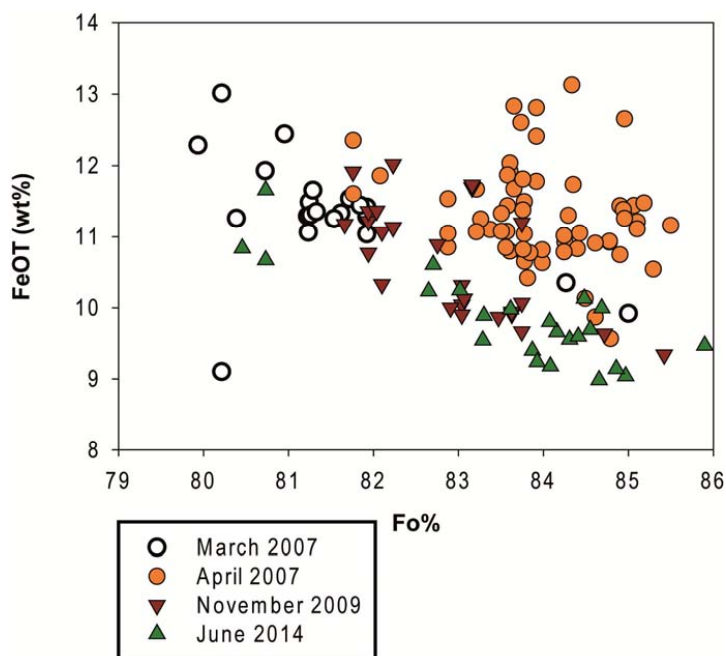
1187 **Figure 7** Ni-Cr concentration plot. (a) Ni-Cr signature of the June 2014 lavas compared to  
 1188 that of recent eruptions (Di Muro et al. (2015) and unpublished data). Whole-rock (circles)  
 1189 and glass (triangles) compositions are shown for the June 2014 eruption. Olivine controlled  
 1190 lines are indicated for olivine hosting 1.2 and 0.6 wt.% Cr-spinel. Compositions used for  
 1191 olivine (Ni=1900 ppm, Cr=300ppm), clinopyroxene (Ni=970 ppm, Cr=4800 ppm), and Cr  
 1192 spinel (Ni=1500 ppm, Cr=25%) are inferred from Salaün et al. (2010), Di Muro et al. (2015)  
 1193 and Welsch et al. (2009). (b) Zoom of the Ni-Cr relationship between glass (triangles) and  
 1194 whole-rock (circles) samples from the June 2014 eruption. Fracture I = Western fracture,  
 1195 Fracture II = Upper fracture

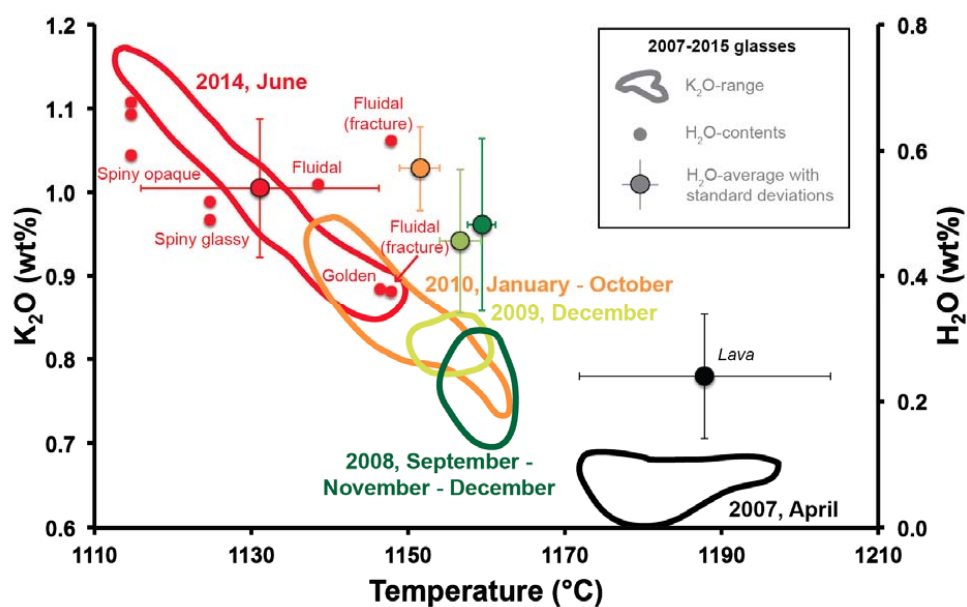


1196

1197 **Fig. 8** (a) Evolution of CaO/Al<sub>2</sub>O<sub>3</sub> ratio in the matrix glasses of recent eruptions at Piton de la  
 1198 Fournaise as a function of MgO content (directly proportional to melt temperature). MI =  
 1199 Melt inclusions (grey area for the 2014 samples). (b) CaO versus MgO content for Piton de la  
 1200 Fournaise products. WR = whole rock, GM = ground mass; MI = melt inclusion, EM =  
 1201 embayment glass

1202





1209

1210 **Figure 10** Temperature, composition (K<sub>2</sub>O) and dissolved water content (H<sub>2</sub>O) for the  
1211 evolution of 2007-2014 melts from glasses. Temperature estimation based on the MgO-  
1212 thermometer of Helz and Thornber (1987) modified by Putirka (2008). Water content from the  
1213 plagioclase hygrometer of Lange et al. (2009). Only plagioclases in equilibrium with melts are  
1214 considered, following the procedure described by Putirka (2008) for >1050°C melts ( $K_d =$   
1215  $0.27 \pm 0.05$ ).

1216

1217

1218

1219

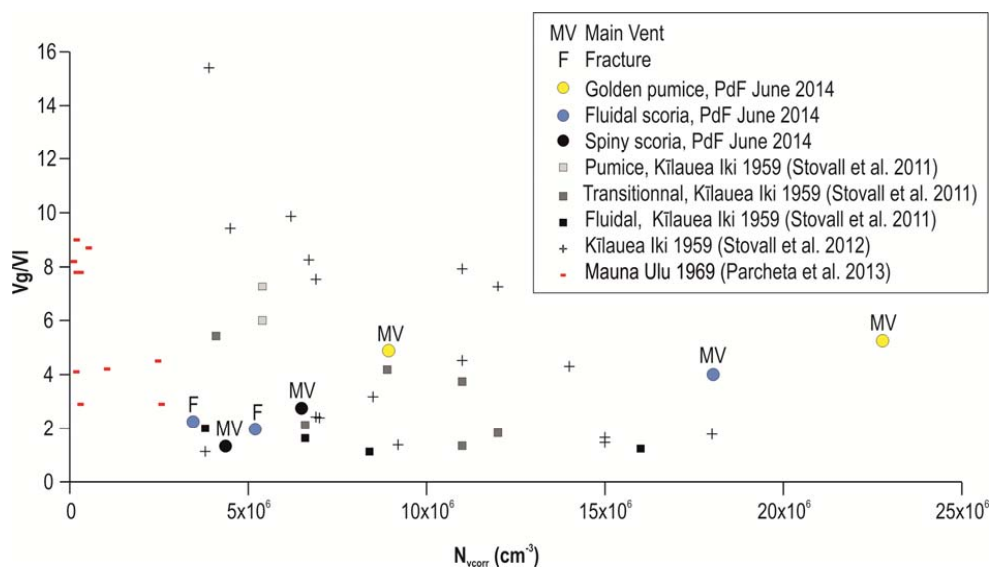
1220

1221

1222

1223

1224



1225

1226 **Figure 11** Volumetric ratio of vesicles to melt (VG/VL) versus vesicle number density

1227

1228